F. Giussani, F. Piscaglia, G. Saez-mischlich, J. Hèlie
*A Three-Phase Vof Solver for the Simulation of In-Nozzle Cavitation Effects on Liquid Atomization*
Journal of Computational Physics, Vol. 406, 2020, 109068 (38 pages)
doi:10.1016/j.jcp.2019.109068

# A three-phase VOF solver for the simulation of in-nozzle cavitation effects on liquid atomization

F. Giussani [a,b,*], F. Piscaglia [a], G. Saez-Mischlich [c], J. Hèlie [b]

[a] Dept. of Aerospace Science and Technology (DAER), Politecnico di Milano, Italy
[b] Continental Automotive SAS, France
[c] ISAE-SUPAERO, Université de Toulouse, France

A B S T R A C T

The development of a single-fluid solver supporting phase-change and able to capture the evolution of three fluids, two of which are miscible, into the sharp interface capturing Volume of Fluid (VOF) approximation, is presented. The transport of each phase-fraction is solved independently by a flux-corrected transport method to ensure the boundedness of the void fraction over the domain. The closure of the system of equations is achieved by a cavitation model, that handles the phase change between the liquid and the fuel vapor and it also accounts for the interaction with the non-condensable gases. Boundedness and conservativeness of the solver in the transport of the volume fraction are verified on two numerical benchmarks: a two-dimensional bubble rising in a liquid column and a cavitating/condensing liquid column. Finally, numerical predictions from large-eddy simulations are compared against experimental results available from literature; in particular, validation against high-speed camera visualizations and Laser Doppler Velocimetry (LDV) measurements of cavitating microscopic in-nozzle flows in a fuel injector is reported.

## 1. Introduction

Cavitation plays a pivotal role in achieving finer atomization of spray to favor an improved fuel economy and reduced emission levels during combustion [1,2]; however, it may also cause a significant reduction in the nozzle volumetric efficiency and in the stability of the spray [3] and to potential damage of the injector components, leading to reduced reliability of the injector. In injector nozzles, after a surface spot is initially surrounded by a cavitating flow region, it tends to erode at an accelerated pace: cavitation pits increase the turbulence of the flow and create crevices that act as nucleation sites for new cavitation bubbles, thus leading to an avalanche effect. From high speed camera visualizations on transparent glass nozzles, two different forms of cavitations have been distinguished [4,5] and they are known as “geometry-induced” and “vortex” (or string) cavitation respectively. Geometry-induced cavitation is initiated at sharp corners where the pressure falls below the saturation value [6–8] because of a sudden flow detachment and the accompanying recirculation region. String (or vortex) cavitation, conversely, develops by the evolution of the vorticity which allows the formation of geometry-scale vortices and is significantly influenced by the walls and the interaction with other vortices [9]; additionally, low pressure regions in the centers of the vortices in the nozzle can generate a phase-change or entrap and stabilize bubbles that were

* Corresponding author at: Dept. of Aerospace Science and Technology (DAER), Politecnico di Milano, Italy.
*E-mail address:* filippo.giussani@polimi.it (F. Giussani).

entrained in their proximity, similarly to what is observed in hydromachines [10,11]. Vortex cavitation in the injector nozzles was first observed by Kim [12] and since then it has been described in further studies performed in enlarged nozzle replicas and was termed as “string cavitation” [13,14]. The main differences between vortex cavitation in propellers and turbines and those in fuel injectors arise from the geometric configuration of the nozzle and the operating conditions of the flow. String cavitation in nozzle flows develops in very confined volumes, that may allow formation of large-scale vortices relative to the nozzle geometry, where each cavitating vortex may interfere with other vortices and where the influence of the walls can be significant. Also, huge pressure drops in fuel injectors are encountered within very short distances (few hundreds of micrometers) while the lifetime of the formed vortical structure is usually only a fraction of the injection period. Cavitation strings are usually formed during fuel injection in areas where large-scale vortical structures develop: this happens when local pressure level is lower than the vapor pressure of the fuel. In a typical nozzle geometry, cavitation vortices are located between the separation point on the needle surface and the separation point at the hole inlet corner, and where there is sharp flow turning inside the sac volume of the injector. Unlike geometrical cavitation, string cavitation is present in any nozzle geometry: with sac-type and Valve Covered Orifice-type (VCO) nozzles, with either cylindrical or tapered holes, whose inlet can be either sharp or rounded. Cavitation modeling in high-pressure injection involves the simulation of multiphase (in the context of this paper refers to liquid and gas) and multicomponent (several instances of the same phase) flows and poses great challenges. These challenges are due to the presence of the interfaces between phases and large or discontinuous properties variations across interfaces between phases and/or components; additionally, the modeling of small-scale interactions between phases and components has a significant impact on macroscopic flow properties, this is why LES turbulence modeling is often required. Two approaches are commonly used for the simulation of multiphase and multicomponent flows. In the first approach, each phase and/or component is considered to fill a distinct volume and the interfaces between the phases and/or components are captured explicitly. This approach is a generalization of two-fluid approach [15]; typical applications [16–18] include the prediction of the motion of large bubbles in a liquid, the motion of liquid after a dam break, the prediction of jet breakup, and the capture of any liquid-gas interface. The mutual interaction at the interface can be described as an interfacial momentum transfer and, when interfacial mass and energy transfer are involved, they also need to be included in the equation sets. In order to model the transfer of mass for cavitation with a minimum set of equations for closure, an equation of state to correlate density and speed of sound with pressure and temperature is required: no additional transport equations are used for the vapor phase, whose void fraction is determined by the mixture composition. Similarly to barotropic models, the density is a function of pressure only. In the second approach, the phases and/or components are spatially averaged to lead to a homogeneous mixture; relative velocity among the phases is neglected, which implies the absence of closure for the transfer of mass, momentum and energy at the interfaces while thermal equilibrium among the different phases is usually assumed. These methods are generally identified by the Volume of Fluid (VOF) [19], the Level Set (LS) [20] and the Coupled Level Set-Volume of Fluid (CLSVOF) [21–23]. The number of phase fraction equations solved can vary depending on the number of fluid interfaces to capture. Fluid properties, such as density and viscosity, sharply vary across the interface of the different phases; finally, the rate of the transfer of mass is controlled by source term built on Rayleigh-Plesset equation [24–27]. Several attempts have been done to combine the potentiality of the VOF with the simplicity of mixture model. In [28] the cavitating fluid mixture (liquid and vapor) is considered as primary phase while the non-condensable gas is the secondary phase; in this case, only one interface is captured by solving the phase-fraction equation for the non-condensable (NC) gas and the void fraction of the cavitating fluid mixture is equal to $(1-\alpha_{nc})$; the volume fraction of the fuel vapor in the cavitating fluid mixture is estimated from the mixture composition, where the densities of the different components are computed through non-linear equations of state. In [29], a mass transfer model published in [30] was extended to an eight-equation two fluid-model to include non-condensable gases. Other methods to describe a three-phase flow while considering non-condensable gases are the use of the homogeneous mixture model combined with a barotropic two-fluid cavitation model [31], or the coupling of a two-fluid approach with VOF [32]. In the latter case, a two-fluid approach is used to describe the interaction between liquid and vapor in the nozzle, while VOF is used to model the jet formation. All the mentioned models have in common the aspect that they capture a single interface between the non-condensable gases and a multi-component mixture [33,34]. Barotropic models are widely used for complex simulations because they are simple to implement and numerically stable. On the other hand, one of the main limitations using a barotropic equation of state is in the underestimation of the vorticity change, because it does not account for the misalignment between the gradient of pressure and the gradient of density $(\nabla\rho\times\nabla p)/\rho^2$ [35], unless a non-linear correlation between pressure and density is used [33]. This contribution, called baroclinity, is important either in compressible fluids and also in incompressible and inhomogeneous fluids and it is identified by the interface in a VOF method. Another challenge when cavitation is modeled using barotropic models is in the definition of an appropriate equation of state for the mixture, which includes air in addition to liquid and vapor. Capture the interface between coexisting miscible phases (fuel vapor and non-condensable gases in this work) in injector nozzles may be important in presence of swirl cavitation and hydraulic flip regime [36,37], when a severe detachment of flow pockets [37,38] transported away from the hole allows non-condensable gases to flow back into the nozzle. This happens both in simplified, straight, central hole injectors [39] and in non-axial nozzles, in which large pressure fluctuations are observed in the nozzle. Recently, attempts to extend VOF, in order to include air in transport and in cavitation model have been done [40], [41] where each phase is considered as a compressible fluid but the cavitation model used [42,43] have been previously developed under incompressible formulation. Conversely, in [44] each phase is considered incompressible and isothermal but the change of density is addressed at the interface and keeps in consideration the presence of the air

inside cavitation model. A multi-fluid quasi-VOF model with the transport of three phases has been proposed also in [45], considering different velocities among phases and thus momentum transfer rate among interfaces. Although several authors have developed different methodologies to describe cavitation and the jet formation, any simple benchmark has not been found in literature in order to provide any further information about the mass conservation guaranteed by the cavitation model, either using the Rayleigh-Plesset equation [24,27] or using a barotropic equation of state coupled with vapor quality. Some tests have been performed using a shock tube or Rayleigh bubble collapse test case [46–49], which deal with surface capture regardless of mass conservation when the phase change occurs.

The objective of this study is to present the development of a three phase VOF solver for three incompressible fluids (liquid fuel, fuel vapor and non-condensable gases), two of which are miscible, where fuel cavitation/condensation is modeled through the Rayleigh-Plesset equation. Three different test cases are proposed for the solver validation: a) a modified version of the test case presented in [50,51] to explore the accuracy of the solver in capturing three interfaces without phase change. Different formulations to compute the surface tension in the VOF method have been investigated and a comparison among them has been shown; b) a novel one-dimensional test case, that consists of a 1D column half filled with liquid, where non-condensable gas (air) stays above the liquid. The hydrostatic pressure field resulting from the weight force of each fluid in quiescent state produces a pressure gradient $\Delta p$ at the interface, letting the onset of cavitation in the liquid. Later on, condensation of the vapor is enforced to reach the initial state. The relative mass conservation error is monitored, together with other relevant quantities, to prove the conservativeness of the solver; c) the three-dimensional internal-nozzle flow of an injector, whose experimental results are available in the literature at one operating point [52]. The discretization of the governing equations used in this study is based on the finite-volume approach as implemented in OpenFOAM [53]. Mass and momentum are solved using the pressure-implicit split-operator (PISO) algorithm [54]. The cavitation and the condensation term have been included in a semi-implicit formulation of the phase-fraction equations, where a flux corrected transport technique [55] is used to preserve boundedness of the solution; cavitation modeling follows the theory by Schnerr and Sauer [43] with the extensions proposed by Yuan [56]. The implemented three-phase solver is able to capture the interface of three phases, namely the liquid, the condensable gas (vapor) and the non-condensable gas (air). Turbulence is modeled using LES: large turbulent scales are resolved, while smaller scales are modeled [57–59]. This separation of scales is explicitly or implicitly [60,61] obtained by filtering out the small flow scales that cannot be properly represented by the mesh [57]; their effect must be modeled on the filtered field by means of the so called subgrid-scale (SGS) model. Although the multiphase nature of the problem, the use of LES models is also very popular in multi-phase single-fluid VOF simulations [62–67]. It is worth mentioning that several numerical studies have been led with Unsteady Reynolds Averaged Naviers Stokes (URANS) equations but this approximation can significantly underestimate the formation and the extent of cavitation due to an overestimated turbulent viscosity in the cavitating zones [68–72]. A comparative study between URANS and LES models [46] shows that URANS models fail to predict the incipient cavitation when the inlet flow pressure is not far from the pressure at the nozzle outlet, while LES is able to better capture the cavitation onset thanks to a better characterization of the different flow scales. A possible solution to overcome the limitations of URANS when applied to cavitation modeling consists in reducing the eddy-viscosity predicted by the turbulence model [68]; this approach looks promising, but its validity does not seem general; LES looks therefore to be the best approach for the problem discussed, despite of its high computational cost.

The paper is organized as follows: the theory of the three phase solver with phase change is discussed from Sec. 2 to Sec. 5; the discretized solution of the phase fraction equations in presence of phase-change, and its coupling to the segregated solution of the governing equations is presented in Sects. 6, 7 and Sec. 8. Then, the rising bubble test case [50] and a new one-dimensional liquid-column benchmark test case have been used for validation in Sects. 10 and 11. Finally, the simulation of a three-dimensional internal nozzle flow and its validation is presented in Sec. 12. Main conclusions are summarized in Sec. 13.

## 2. Phase-fraction equations in the VOF solver

The cavitating fluid, the vapor and the non-condensable gas in the three-phase flow are represented in a single-fluid approximation as a mixture of phases, in which the phase-fraction distribution includes a sharp yet resolved transition between the phases.

An algebraic-type VoF method belonging to the family of the interface-capturing methods [73], is used to capture the interface; more specifically, the interface is visualized by the contour of a scalar function, that is assumed to be the iso-value (set to 0.5 in this work) of the void fraction of the phase considered. Each phase $i$ has a partial volume $V_i$, that is a fraction of the volume $V$ of the cell element ($V_i \subseteq V$) and it is defined by its local volume fraction $\alpha_i \in [0;1]$:

$$\alpha_i = \frac{V_i}{V} \tag{1}$$

with:

$$\sum_{i=1}^{3} \alpha_i = 1 \tag{2}$$

a “mixture” density:

$$\rho = \sum_i \alpha_i \rho_i \tag{3}$$

and a “mixture” viscosity:

$$\mu = \sum_i \alpha_i \mu_i \tag{4}$$

It is important to note that density in the solver varies with pressure, through the phase transport equations. The effect of the heat transfer on the temperature, that should be accounted by solving the energy equation, is not considered in the present work. The complete system of equations for three-phase flow with phase change are the phase-fraction equations, that are written as:

$$\begin{cases} \dfrac{\partial \alpha_l}{\partial t} + \nabla \cdot (\mathbf{U}\alpha_l) = -\dfrac{S_\alpha}{\rho_l} \\ \dfrac{\partial \alpha_v}{\partial t} + \nabla \cdot (\mathbf{U}\alpha_v) = \dfrac{S_\alpha}{\rho_v} \\ \dfrac{\partial \alpha_{nc}}{\partial t} + \nabla \cdot (\mathbf{U}\alpha_{nc}) = 0 \end{cases} \tag{5}$$

In the system of equations (5), $S_\alpha$ is a source term to model the phase-change (cavitation or condensation) at the liquid interface through the cavitation model and couples the effects of the cavitation with the evolution of the interface directly:

$$S_\alpha = \frac{\rho_v \rho_l}{\rho + \alpha_{nc}(\rho_l - \rho_{nc})} \frac{D\alpha_v}{Dt} \tag{6}$$

In Eq. (6) the subscripts $l$ and $v$ are adopted for liquid and vapor (that are involved in the phase change) respectively, while the subscript $nc$ is adopted for non-condensable gases. It is important to note that the closure of the system of equations (5) in presence of a cavitation/condensation source term $S_\alpha$ requires to explicitly resolve the transport of a third phase fraction (non-condensable phase), to include a cavitation model and to couple the equations with the compatibility condition (2); in this way, the system is closed and implicitly bounded, thanks to (2). In absence of source terms, 3-phase VOF solvers usually calculate the void fraction of non-condensable gases directly from Eq. (2), that is sufficient for closure only in that case. These aspects are discussed in detail in Appendix A and Appendix B, where the derivation of the full system of equations is shown and the formulation of the source terms for the phase change is also described.

*2.0.1. Counter-gradient transport in VOF*

In the FV framework, numerical diffusion, which is very high in the transport term in second-order spatial discretization, “smears” the sharp liquid-gas interface. In OpenFOAM, the strategy commonly followed in multiphase VOF solvers to model the transport of the void fraction consists in adding a convection term which compresses the interface and preserves boundedness: this is similar to what is done for the treatment of the scalar-flux second-moment closure, used for the “counter-gradient” transport in some complex combustion models describing the dynamic of turbulent flames [74]. In the VOF treatment, a common closure used for counter-gradient transport has the form:

$$\nabla \cdot [\mathbf{U}_c \, \alpha \, (1 - \alpha)] \tag{7}$$

where $\mathbf{U}_c$ is the compression velocity at the interface between the phases, which is a consequence of the different densities and the term $\alpha(1-\alpha)$ ensures boundedness [55]. In the VOF solver used, the compression velocity is modeled as:

$$\mathbf{U}_c = c_\alpha |\mathbf{U}| \hat{\mathbf{n}}_{ij} \tag{8}$$

The employed formulation of the compression velocity is:

$$\mathbf{U}_c = \min\left[c_\alpha |\mathbf{U}|, \max(|\mathbf{U}|)\right] \hat{\mathbf{n}}_{ij} \tag{9}$$

The discretized form of Eq. (7) is a flux (counter-gradient term, Eq. (38)) computed at the cell faces using a Total Variation Diminishing (TVD) scheme. In this work, the TVD scheme used is called `interfaceCompression` scheme [55], in which the limiter $\psi$ to compute the flux is defined as:

$$\psi(\phi_P, \phi_N) = min\left\{max\left[1 - max\left(\sqrt{1 - 4 \cdot \phi_P \cdot (1 - \phi_p)}, \sqrt{1 - 4 \cdot \phi_N \cdot (1 - \phi_N)}\right), 0\right], 1\right\} \tag{10}$$

$\psi$ is bounded between 0 and 1; $\phi_P$ is the value of the variable, defined at the cell center, where the limiter is applied; $\phi_N$ is the value of the same variable in the neighboring cells.

The compression rate should be set in order to ensure interface sharpness. Higher values of the compression rate might introduce numerical instability or slow convergence. The term $C_\alpha$ in Eq. (9) is the compression coefficient and it is set to unity in this work. The compression coefficient $C_\alpha$ is a binary coefficient which switches interface sharpening on ($C_\alpha \geq 1$) or off ($C_\alpha = 0$). With $C_\alpha$ set to 0 for a given phase pair, there is no imposed interface compression resulting in phase dispersion according to the multi-fluid model. If $C_\alpha$ is set to 1, sharp interface capturing is applied and VOF-style phase fraction capturing occurs, forcing interface resolution on the mesh. If a compression term is not applied, the interface will be very diffuse. In most applications, it is suggested a $c_\alpha$ of the order of unity [55]. A complete discussion about the interface compression method and the compression coefficient can be found in [75].

To ensure that the compression term does not bias the solution, it should only introduce flow of $\alpha$, normal to the interface, in the direction of the volume average interface normal $\hat{\mathbf{n}}_{ij}$. For a three-phase solver it has been computed as net gradient of the phase $i$-th at the interface [53]:

$$\hat{\mathbf{n}}_{ij} = \frac{\alpha_j \nabla \alpha_i - \alpha_i \nabla \alpha_j}{\|\alpha_j \nabla \alpha_i - \alpha_i \nabla \alpha_j\|} \tag{11}$$

In the convention adopted (see Fig. 1), $\hat{\mathbf{n}}_{ij}$ always points towards the lighter fluid. A common practice is to use the compression term only where surface sharpness wants to be preserved: in the proposed formulation, the convection-based term is used only to compress the interface between the immiscible (liquid fuel) and the miscible phases (fuel vapor and non-condensable gases). The phase-fraction equations for the three phase VOF take the form:

$$\begin{cases} \dfrac{\partial \alpha_l}{\partial t} + \nabla \cdot (\alpha_l \mathbf{U}) + \underbrace{\nabla \cdot (\alpha_l \alpha_v \mathbf{U}_{c_{lv}}) + \nabla \cdot (\alpha_l \alpha_{nc} \mathbf{U}_{c_{lnc}})}_{\text{compression term, liquid-vapor + liquid-non condensable gases}} = -\dfrac{\rho_v}{\rho + \alpha_{nc}(\rho_l - \rho_{nc})} \dfrac{D\alpha_v}{Dt} \\ \dfrac{\partial \alpha_v}{\partial t} + \nabla \cdot (\alpha_v \mathbf{U}) + \underbrace{\nabla \cdot (\alpha_l \alpha_v \mathbf{U}_{c_{lv}})}_{\text{compression term, liquid-vapor}} = \dfrac{\rho_l}{\rho + \alpha_{nc}(\rho_l - \rho_{nc})} \dfrac{D\alpha_v}{Dt} \\ \dfrac{\partial \alpha_{nc}}{\partial t} + \nabla \cdot (\alpha_{nc} \mathbf{U}) + \underbrace{\nabla \cdot (\alpha_l \alpha_{nc} \mathbf{U}_{c_{lnc}})}_{\text{compression term, liquid-non condensable gases}} = 0 \end{cases} \tag{12}$$

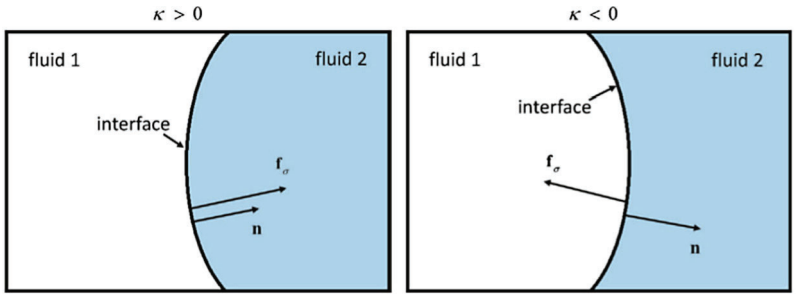


**Fig. 1.** Schematic of the interface between two fluids. $\mathbf{f}_\sigma$ is the surface force per unit inter-facial area; $\hat{\mathbf{n}}$ and $\kappa$ are namely the interface normal and the interface curvature. According to the sign convention adopted, $\mathbf{f}_\sigma$ is always oriented towards the concave interface and $\hat{\mathbf{n}}$ always points towards lighter couple of fluids [76].

In Eqs. (12), no additional terms to model interface compression between miscible phases are used; numerical diffusion is assumed to be sufficient to model the small diffusion of mass at the interface when convection is dominant (i.e. with large values of Reynolds and low Schmidt numbers). Different modeling approaches for sub grid-scale computation of the mass transfer are only proposed for low-Re and high Schmidt number flows [77–79]. The term $\frac{D\alpha_v}{Dt}$ in Eqs. (12) includes the effects of the phase change (cavitation/condensation) and it is therefore linked to the cavitation/condensation model.

## 3. Mass conservation in the VOF solver

During cavitation and condensation, liquid and vapor phase are both affected by a strong variation of density. The latter influences significantly the numerics of the segregated solver. Therefore, to ensure the stability of the solver under the aforementioned condition, the continuity equation is used in its non-conservative form as suggested in [80] and which it has already been used [43,81,44]:

$$\nabla \cdot \mathbf{U} = -\frac{1}{\rho} \frac{D\rho}{Dt} \tag{13}$$

The advantage of using volume fluxes rather than mass fluxes (conservative form) consists of having continuous volume fluxes at the interface, thus favoring the solution of pressure correction equation. With phase change and three phases, Eq. (13) can be rewritten as:

$$\nabla \cdot \mathbf{U} = \frac{\rho_l - \rho_v}{\rho + \alpha_{nc}(\rho_l - \rho_{nc})} \frac{D\alpha_v}{Dt} \tag{14}$$

The derivation of the RHS of Eq. (14) is reported in Appendix A.

## 4. Momentum conservation in the VOF solver

The momentum equation reads:

$$\frac{\partial (\rho \mathbf{U})}{\partial t} + \nabla \cdot (\rho \mathbf{U} \otimes \mathbf{U}) = -\nabla \hat{p} + \nabla \cdot \boldsymbol{\tau} + \mathbf{f}_\sigma + S_U - \mathbf{g} \cdot \mathbf{x} \nabla \rho \tag{15}$$

where $\hat{p}$ is a modified pressure, that is calculated by removing the hydrostatic part from the static pressure $p$, $\boldsymbol{\tau}$ is the deviatoric stress tensor, $S_U$ includes the source terms, $\mathbf{f}_\sigma$ is the surface force per unit inter-facial area calculated at the fluid interface in the control volume, $\mathbf{g}$ is the gravitational acceleration. The term $-\mathbf{g} \cdot \mathbf{x} \nabla \rho$ in the RHS of Eq. (15) is a consequence of the removal of the modified pressure $\hat{p}$ from the static pressure:

$$\hat{p} = p - \rho \mathbf{g} \cdot \mathbf{x} \tag{16}$$

which yields:

$$\nabla \hat{p} = \nabla p - \nabla(\rho \mathbf{g} \cdot \mathbf{x}) = \nabla p - \rho \mathbf{g} - \mathbf{g} \cdot \mathbf{x} \nabla \rho \tag{17}$$

so:

$$-\nabla p + \rho \mathbf{g} = -\nabla \hat{p} - \mathbf{g} \cdot \mathbf{x} \nabla \rho \tag{18}$$

The use of $\hat{p}$ in the momentum equation favors a more stable solution of the density jumps at the sharp interface and simplifies the implementation and setup of the boundary conditions on pressure. In Eq. (15), $\mathbf{f}_\sigma$ is defined as:

$$\mathbf{f}_\sigma = \sigma \, \kappa \, \hat{\mathbf{n}} \, \delta \, (\mathbf{x} - \mathbf{x_s}) \tag{19}$$

where $\sigma$ is the fluid surface tension coefficient in [N/m], $\hat{\mathbf{n}}$ is the unit vector normal to the liquid interface, whose center is located in $\mathbf{x}_s$, $\delta$ is the Dirac function to ensure that the force is applied only at the liquid interface, $\kappa$ is the interface curvature [$\mathrm{m}^{-1}$], which is defined as:

$$\kappa \equiv -\nabla \cdot (\hat{\mathbf{n}} \cdot \mathbf{S}_f) \tag{20}$$

where $\mathbf{S}_f$ is the cell faces surface area vector defined as the scalar product between the cell faces normal and the cell face area. In Eq. (19), $\mathbf{f}_\sigma$ is always oriented towards the concave interface (Fig. 1). It is important to note that the interface curvature in Eq. (19) and (20) used is the one of the interfaces of the phase with highest density (liquid in this case):

$$\hat{\mathbf{n}} = \frac{\nabla \alpha_l}{\|\nabla \alpha_l\|} \tag{21}$$

The surface tension coefficient $\sigma$ appearing in Eq. (19), has been written as an average of the surface tensions weighted with the phase-fractions computed in the control volume:

$$\sigma = \frac{\alpha_v \sigma_{lv} + \alpha_{nc} \sigma_{lnc}}{\alpha_v + \alpha_{nc}} \tag{22}$$

where $\sigma_{lv}$ is the surface tension between the liquid fuel and fuel vapor, while $\sigma_{lnc}$ is the surface tension between liquid fuel and non-condensable gases. Similarly to viscosity and density, the surface tension coefficient $\sigma$ for the mixture is computed as a weighted-average, where the weighting factors are the void fractions; the concept of miscible phases implies that their surface tension coefficient is zero, so $\sigma$ does not include the surface tension between fuel vapor and non-condensable gases. Finally, to compute the surface tension force, the term $\hat{\mathbf{n}} \, \delta \, (\mathbf{x} - \mathbf{x}_s)$ in Eq. (23) must be also modeled. The Continuous Surface Force (CSF) approximation [82] is therefore used, yielding to:

$$\mathbf{f}_{\sigma_i} = \sigma \kappa \nabla \alpha_i \tag{23}$$

It must be remarked that CSF is the simplest model commonly used in VOF solvers. Despite its popularity, it has been proven (in surface tension dominated/driven flow) that it does not guarantee momentum conservation [83], leading to the onset of physically unrealistic velocities at the interface. This parasitic current can be relevant when the flow is highly

dominated by surface tension forces. For that reason, several different formulations as the Continuum-Surface-Stress (CSS) approximation [84] and the Ghost fluid Method (GFM) [85] have been proposed. The former is based on the integral formulation rather than on the volumetric one, and gives more advantages such as inclusion of the tangential stresses due to a variable surface tension (i.e. Marangoni Effect). However, since it was only applied within high-order (spline-based) front-tracking interface description framework [86,87], CSF is rather preferred for its simplicity, especially if surface tension is not dominant. On the contrary, the GFM is a technique used to handle sharp transitions and in the case of capillary forces, it explicitly introduces the singular pressure jump condition into the discretization equations. Each phase is then artificially extended across the interface, producing ghost cells which contain properties of the extrapolated phase used for the discretization scheme, removing the tendency for the adjacent inter-facial cells to diffuse due to the sharp transition. This method has been also extended by several authors [88–90] but always based on LS and CLSVOF since they can compute in a more accurate way the interface curvature [91].

If LES-specific filtering operations are applied to the momentum and to the phase-fraction equations in a single-fluid multiphase solver, additional sub-grid terms appear. These terms can be identified under the so called interface-specific sub-grid contributions. The term coming from the filtering applied to the term representing the surface tension forces ($\mathbf{f}_{\sigma_i} = \sigma\kappa\nabla\alpha_i$) in the momentum equation is a Sub-grid Curvature Tensor (SCT); while terms coming from the filtering of the phase advection terms ($\nabla\cdot(\mathbf{U}\alpha_i)$) are known as Sub-grid Mass Transfer terms (SMT). Published works on two-phase flow interfacial flows without phase-change [92–94] proved that in specific flow configurations [92], those sub-grid terms cannot be neglected. At least three possible closure terms have been published to model the Sub-grid Curvature Tensor: the Sub-Grid Surface Dynamics (SGSD) model [95], the Sub-grid curvature model [96] and the ADM-$\tau$ [97,98]. No works have been found by the authors where the Sub-grid Mass Transfer term has been modeled, even if in [92,99] it is reported that in some cases (like the "separation of phase" test case) it may have the same order of magnitude of the filtered resolved advection term. On the other hand, the vapor phase-fraction $\alpha_v$ is hardly subject to high-frequency fluctuation according to the definition of Eq. (B.5), because the pressure fluctuations only acts directly on the time-derivative of the bubble radius R [65]. Since cavitation is modeled by several micro-bubbles, their status is little sensitive to pressure pulsation rather than to the mean pressure distribution; for this reason, the sub-grid scale related to the SMT should be negligible with respect to the filtered vapor volume fraction field in the cavitation regions where the mean pressure is relatively uniform. Moreover, in the flow regions with sharp pressure gradient, the vapor volume fraction is itself small enough to allow SMT to be neglected. It must be underlined that, the proposed closure terms for SCT have been developed for explicit filtering approach; when deconvolution is performed, the velocity obtained is not strictly equal to $\mathbf{U} = \overline{\mathbf{U}} + \mathbf{U}_{sgs}$, being the deconvolution operator approximated. Finally, the "separation of phase" test [92], used for the sub-grid interface analysis, is dominated by the surface tension forces effects. According to authors' research, no published works studied the contribution of the sub-grid interface with high speed flows including phase-change: such a study would therefore represent a big step towards an improved mathematical description of the formulation of LES single-fluid VOF solvers with phase-change. It is worth to remind that in the Finite Volume (FV) approach, both the computational grid and the discretization of the operators implicitly act as a top-hat filter to the equations [100]. Since most of the CFD solvers in the FV framework are usually limited to second order accuracy [101], the SCT and the SMT term coming from filtering of the equations would be probably biased by the discretization schemes and by the grid [102,103], even when explicit filtering is applied.

The filtering procedure would produce another additional term in the phase-fraction equations (Eqs. (12)) with phase-change. However, no information about these terms was found in literature.

## 5. Cavitation model

Cavitation may consist either of small bubbles (bubbly-flow cavitation) or may contain large pockets of vapor (cloud cavitation) [104]; with a sharp interface-capture method, the bubble must be larger than the cell to be accurately resolved, otherwise a sub-model is needed. In the approach followed in this work, a sub-model for cavitation is always used to provide an expression for the term $\frac{D\alpha_v}{Dt}$. This is required to close the system of governing equations (12), (14) and (15). The rates of fuel vaporization and condensation are determined by a simplification of the Rayleigh-Plesset equation which assumes spherical bubbles of radius $R$ subject to uniform pressure variations. Spherical bubbles are then represented by a fraction of the vapor phase in the computational cell; from [81] and considering that liquid, vapor and non-condensable gases may coexist in a control volume, it follows:

$$V_v = N_b\frac{4}{3}\pi R^3 = n_0 V_l\frac{4}{3}\pi R^3 \tag{24}$$

where $V_v$ and $V_l$ are respectively the volume of the vapor and the liquid in the computational cell of volume V, $N_b$ is the number of spherical bubbles of radius $R$ in the computational cell and $n_0$ is defined as the bubble concentration per unit volume of pure liquid. The use of relations of Eq. (24) requires an a-priori knowledge of the nuclei concentration $n_0$ and an estimation of their initial radius $R$. Some measurements of cavitation nuclei were carried out a few decades ago on water using Cavitation Susceptibility Meter (CSM) and Holographic measurement [105]; even though the holographic

measurements have proved to be more accurate than CSM, both techniques cannot detect bubbles at the sub-micrometer scale and they may omit many additional nuclei. In addition, the growth of the smallest bubbles is affected by the surface tension, that is not considered [25] to have a simple correlation describing the bubble growth. A proper estimation of the surface tension would require a numerical approach to determine the bubble growth rate, but it would require a significant increase of the computational cost [25]. Nucleation can be originated either by homogeneous and by heterogeneous nuclei as well (air dissolved in the liquid, particles, etc.) [104,106]. For the sake of simplicity, only homogeneous nuclei have been considered in the present model; as a consequence, it is not straightforward to set the value of this parameter for the case of high-pressure injection, since measurements of nuclei are not available in literature. For fuel injection, it is usually accepted that the number of nuclei, due to impurities, are large enough that they should not influence the results of the model. Dissolved gas could also contribute [107], but as a first step, in the present study they are not considered as nucleon precursors. The complete expression for the rate of fuel vaporization, derived in Appendix B, is:

$$\frac{D\alpha_v}{Dt} = \begin{cases} \dfrac{3\alpha_v \frac{DR}{Dt}}{R+R^4\frac{4}{3}\pi n_0\left[\frac{\rho+\alpha_{nc}(\rho_v-\rho_{nc})}{\rho+\alpha_{nc}(\rho_l-\rho_{nc})}\right]} = -\dfrac{3\alpha_v max(p-p_{sat},0)\sqrt{\frac{2}{3}\frac{1}{\rho_l\lvert p-p_{sat}\rvert}}}{R+R^4\frac{4}{3}\pi n_0\left[\frac{\rho+\alpha_{nc}(\rho_v-\rho_{nc})}{\rho+\alpha_{nc}(\rho_l-\rho_{nc})}\right]} = \alpha_v\left(\frac{D\alpha_v}{Dt}\right)^+ & if\ p > p_{sat} \\ \dfrac{\alpha_l 4\pi n_0 R^2 \frac{DR}{Dt}}{1+R^3\frac{4}{3}\pi n_0\left[\frac{\rho+\alpha_{nc}(\rho_v-\rho_{nc})}{\rho+\alpha_{nc}(\rho_l-\rho_{nc})}\right]} = -\dfrac{\alpha_l 4\pi n_0 R^2 min(p-p_{sat},0)\sqrt{\frac{2}{3}\frac{1}{\rho_l\lvert p-p_{sat}\rvert}}}{1+R^3\frac{4}{3}\pi n_0\left[\frac{\rho+\alpha_{nc}(\rho_v-\rho_{nc})}{\rho+\alpha_{nc}(\rho_l-\rho_{nc})}\right]} = \alpha_l\left(\frac{D\alpha_v}{Dt}\right)^- & if\ p < p_{sat} \end{cases} \tag{25}$$

which can be rewritten as a net contribution between cavitation and the condensation:

$$\frac{D\alpha_v}{Dt} = \left(\frac{D\alpha_v}{Dt}\right)^+ \alpha_v + \left(\frac{D\alpha_v}{Dt}\right)^- \alpha_l \tag{26}$$

In the transport equation for the liquid phase $\alpha_l$ in the system (12) $\frac{D\alpha_v}{Dt}$ is replaced by rewriting Eq. (26) in the form:

$$\begin{aligned} \frac{D\alpha_v}{Dt} &= \left(\frac{D\alpha_v}{Dt}\right)^+ \alpha_v + \left(\frac{D\alpha_v}{Dt}\right)^- \alpha_l \\ &= \left(\frac{D\alpha_v}{Dt}\right)^+ (1-\alpha_{nc}-\alpha_l) + \left(\frac{D\alpha_v}{Dt}\right)^- \alpha_l \\ &= \left[\left(\frac{D\alpha_v}{Dt}\right)^- - \left(\frac{D\alpha_v}{Dt}\right)^+\right]\alpha_l + \left(\frac{D\alpha_v}{Dt}\right)^+ (1-\alpha_{nc}) \end{aligned} \tag{27}$$

while in the transport equation of the vapor phase $\alpha_v$, still in the system (12), Eq. (26) is manipulated to write $\frac{D\alpha_v}{Dt}$ in the form:

$$\begin{aligned} \frac{D\alpha_v}{Dt} &= \left(\frac{D\alpha_v}{Dt}\right)^+ \alpha_v + \left(\frac{D\alpha_v}{Dt}\right)^- \alpha_l \\ &= \left(\frac{D\alpha_v}{Dt}\right)^+ \alpha_v + \left(\frac{D\alpha_v}{Dt}\right)^- (1-\alpha_v-\alpha_{nc}) \\ &= \left[\left(\frac{D\alpha_v}{Dt}\right)^+ - \left(\frac{D\alpha_v}{Dt}\right)^-\right]\alpha_v + \left(\frac{D\alpha_v}{Dt}\right)^- (1-\alpha_{nc}) \end{aligned} \tag{28}$$

Both in Eq. (27) and (28), the first term in the square brackets is the coefficient of a part of the equation that will be implicitly solved, while the remaining part is explicitly solved. As it will be explained in the further sections, solving the source term in a semi-implicit fashion favors improved numerical stability and boundedness. The final form of the system describing the transport of the three phase fractions reads:

$$
\begin{cases}
\dfrac{\partial \alpha_l}{\partial t} + \nabla \cdot (\alpha_l \mathbf{U}) + \underbrace{\nabla \cdot (\alpha_l \alpha_v \mathbf{U}_{c_{lv}}) + \nabla \cdot (\alpha_l \alpha_{nc} \mathbf{U}_{c_{lnc}})}_{\text{compression term, liquid-vapor + liquid-non condensable gases}} \\
\quad = -\dfrac{\rho_v}{\rho + \alpha_{nc}(\rho_l - \rho_{nc})} \left\{ \left[ \left( \dfrac{D\alpha_v}{Dt} \right)^- - \left( \dfrac{D\alpha_v}{Dt} \right)^+ \right] \alpha_l + \left( \dfrac{D\alpha_v}{Dt} \right)^+ (1 - \alpha_{nc}) \right\} \\
\dfrac{\partial \alpha_v}{\partial t} + \nabla \cdot (\alpha_v \mathbf{U}) + \underbrace{\nabla \cdot (\alpha_l \alpha_v \mathbf{U}_{c_{lv}})}_{\text{compression term, liquid-vapor}} \\
\quad = \dfrac{\rho_l}{\rho + \alpha_{nc}(\rho_l - \rho_{nc})} \left\{ \left[ \left( \dfrac{D\alpha_v}{Dt} \right)^+ - \left( \dfrac{D\alpha_v}{Dt} \right)^- \right] \alpha_v + \left( \dfrac{D\alpha_v}{Dt} \right)^- (1 - \alpha_{nc}) \right\} \\
\dfrac{\partial \alpha_{nc}}{\partial t} + \nabla \cdot (\alpha_{nc} \mathbf{U}) + \underbrace{\nabla \cdot (\alpha_l \alpha_{nc} \mathbf{U}_{c_{lnc}})}_{\text{compression term, liquid-non condensable gases}} = 0
\end{cases}
\tag{29}
$$

## 6. Solution algorithm

The code resolves the governing equations by the Finite Volume (FV) Solution Method; a cell-centered formulation with co-located arrangement is used for the sequential solution of the governing equations on a polyhedral mesh. The segregated solution of the governing equations (mass and momentum) is achieved by a pressure-velocity coupling algorithm. The turbulent viscosity $\mu_t$ is modeled using the Wall-Adapting Local Eddy-viscosity model (WALE) [108], which has been proved to be suitable for wall-bounded flows and single-fluid approach [9].

## 7. Discretized form of the phase-fraction equations

The solver has been developed in order to model high-speed injection and primary atomization. This a very challenging task for interface tracking and capturing methods. In this regard, the most important factor that must be considered is the mutual effect of turbulence and cavitation. Breakup and cavitation processes are dominated by surface instabilities, which are affected by turbulence, by the boundary conditions and by the numerics. Turbulence in the liquid, and to a lesser extent in the gas phase, strongly influences the predictions in the injection breakup; the fact that surface structures being resolved are of a similar space and time-scale to small, but not the smallest, turbulent structures suggests that this interaction cannot be realistically represented by traditional RANS modeling and that LES turbulence is the most appropriate approach. The use of LES imposes tight constraints on the numerics in the case setup: high resolution schemes and accurate numerics are required for differentiation, in order to preserve the energy associated with the resolved turbulent structures and to avoid a numerical error working as artificial dissipation [102]. On the other hand, high-order methods applied to high-speed flows in complex geometries may lead to instabilities; for this reason, special care must be taken in the discretization of the convection of momentum and of the temporal derivatives. In particular, the numerical fluctuation created by the VOF approach, possibly coming from the compression and mostly from the cavitation/condensation source terms, are preserved by second-order time-differencing schemes; as a result, a wrong accumulation of energy may be found and, in turn, the simulation is destabilized. The stencil of the discretization for the phase-fraction equations of system (29) makes use of a first-order time differencing scheme, as it happens when first order hyperbolic PDE are used [109]:

$$
\begin{cases}
\dfrac{(\alpha_l^{n+1} - \alpha_l^n)_p}{\Delta t} V_p + \sum_f F_f^n = B_{l_p}^n \left[ \left( \dfrac{D\alpha_v}{Dt} \right)^- - \left( \dfrac{D\alpha_v}{Dt} \right)^+ \right]_p^n \alpha_{l_p}^{n+1} V_p + B_{l_p}^n \left[ \left( \dfrac{D\alpha_v}{Dt} \right)^+ \right]_p^n (1 - \alpha_{nc})_p^n V_p \\
\dfrac{(\alpha_v^{n+1} - \alpha_v^n)_p}{\Delta t} V_p + \sum_f F_f^n = B_{v_p}^n \left[ \left( \dfrac{D\alpha_v}{Dt} \right)^+ - \left( \dfrac{D\alpha_v}{Dt} \right)^- \right]_p^n \alpha_{v_p}^{n+1} V_p + B_{v_p}^n \left[ \left( \dfrac{D\alpha_v}{Dt} \right)^- \right]_p^n (1 - \alpha_{nc})_p^n V_p \\
\dfrac{(\alpha_{nc}^{n+1} - \alpha_{nc}^n)_p}{\Delta t} V_p + \sum_f F_f^n = 0
\end{cases}
\tag{30}
$$

where the subscript $P$ in the equations indicates that quantities are defined at the center of the Control Volume (CV); $\sum_f F_{i,f}$ is the sum of the convective fluxes for the $i$-th phase (see Sec. 8) and:

$$
B_{l_p}^n = \left[ -\frac{\rho_v}{\rho + \alpha_{nc}(\rho_l - \rho_{nc})} \right]_p^n \tag{31}
$$

$$B_{v_p}^n = \left[ \frac{\rho_l}{\rho + \alpha_{nc}(\rho_l - \rho_{nc})} \right]_p^n \tag{32}$$

System of equations (30) is then solved explicitly as follows:

$$\begin{cases} \alpha_{l_p}^{n+1} = \dfrac{\alpha_{l_p}^n - \sum_f F_{i,f}^n \frac{\Delta t}{V_p} + B_{l_p}^n \left[ \left( \frac{D\alpha_v}{Dt} \right)^+ \right]_p^n (1-\alpha_{nc})_p^n \Delta t}{1 - B_{l_p}^n \Delta t \left[ \left( \frac{D\alpha_v}{Dt} \right)^- - \left( \frac{D\alpha_v}{Dt} \right)^+ \right]_p^n} \\ \alpha_{v_p}^{n+1} = \dfrac{\alpha_{v_p}^n - \sum_f F_{i,f}^n \frac{\Delta t}{V_p} + B_{v_p}^n \left[ \left( \frac{D\alpha_v}{Dt} \right)^- \right]_p^n (1-\alpha_{nc})_p^n \Delta t}{1 - B_{v_p}^n \Delta t \left[ \left( \frac{D\alpha_v}{Dt} \right)^+ - \left( \frac{D\alpha_v}{Dt} \right)^- \right]_p^n} \\ \alpha_{nc_p}^{n+1} = \alpha_{nc_p}^n - \dfrac{\Delta t}{V_p} \sum_f F_{i,f}^n \end{cases} \tag{33}$$

Total Variation Diminishing (TVD) [110] is applied in the calculation of $\alpha_{l_p}^{n+1}$ and $\alpha_{v_p}^{n+1}$, to ensure a stable solution and boundedness of the phase fraction with large density ratios. In this way, the oscillations in the solution near discontinuities in the phase-fraction equations (represented by the interface of the VOF) are smoothed and monotonicity is preserved. Phase transition leads to large values of the fluxes: this is particularly apparent in the calculation of the transport equation for the liquid phase. It has a direct effect on the stability of the solver and may put constraints in the time-step advancement. Similar considerations may be drawn for the transport equation of the vapor phase, but in this case the contribution on the fluxes deriving from the phase transition (condensation) is not so large as for the liquid and a bounded solution can be achieved. To stabilize the solution of the transport equation for the liquid fraction in (29), the term $\alpha_l \nabla \cdot \mathbf{U}$ is added and subtracted on its RHS. The equation is then written as:

$$\begin{aligned} \frac{\partial \alpha_l}{\partial t} + \nabla \cdot (\mathbf{U}\alpha_l) + \nabla \cdot (\mathbf{U}_{c_{lv}} \alpha_l \alpha_v) + \nabla \cdot (\mathbf{U}_{c_{lnc}} \alpha_l \alpha_{nc}) &= -\frac{\rho_v}{\rho + \alpha_{nc}(\rho_l - \rho_{nc})} \frac{D\alpha_v}{Dt} - \alpha_l \nabla \cdot \mathbf{U} + \alpha_l \nabla \cdot \mathbf{U} = \\ &= -\frac{\rho_v}{\rho + \alpha_{nc}(\rho_l - \rho_{nc})} \frac{D\alpha_v}{Dt} - \alpha_l \frac{\frac{D\alpha_v}{Dt}(\rho_l - \rho_v)}{\rho + \alpha_{nc}(\rho_l - \rho_{nc})} + \alpha_l \nabla \cdot \mathbf{U} = \\ &= \frac{D\alpha_v}{Dt} \frac{\rho_l \rho_v}{\rho + \alpha_{nc}(\rho_l - \rho_{nc})} \left[ -\frac{1}{\alpha_l} + \alpha_l \left( \frac{1}{\rho_l} - \frac{1}{\rho_v} \right) \right] + \alpha_l \nabla \cdot \mathbf{U} = \\ &= \frac{D\alpha_v}{Dt} \frac{\rho_l \rho_v}{\rho + \alpha_{nc}(\rho_l - \rho_{nc})} A_l + \alpha_l \nabla \cdot \mathbf{U} \end{aligned} \tag{34}$$

The discretized form of Eq. (34) reads:

$$\begin{aligned} \frac{(\alpha_l^{n+1} - \alpha_l^n)_p}{\Delta t} V_p + \sum_f F_f^n = B_{l_p}^n &\left[ \left( \frac{D\alpha_v}{Dt} \right)^- - \left( \frac{D\alpha_v}{Dt} \right)^+ \right]_p^n \alpha_{l_p}^{n+1} V_p \\ &+ B_{l_p}^n \left[ \left( \frac{D\alpha_v}{Dt} \right)^+ \right]_p^n (1-\alpha_{nc})_p^n V_p + \alpha_{l_p}^n \sum_f \mathbf{U}_f^n \cdot \mathbf{S}_f \end{aligned} \tag{35}$$

where

$$B_{l_p}^n = \left[ \frac{\rho_l \rho_v}{\rho + \alpha_{nc}(\rho_l - \rho_{nc})} A_l \right]_p^n \tag{36}$$

The final expression to calculate the liquid fraction $\alpha_l^{n+1}$ in (29) is:

$$\alpha_{l_p}^{n+1} = \frac{\alpha_{l_p}^n \left(1 + \sum_f \mathbf{U}_f^n \cdot \mathbf{S}_f \frac{\Delta t}{V_p}\right) - \sum_f F_f^n \frac{\Delta t}{V_p} + B_{l_p}^n \left[\left(\frac{D\alpha_v}{Dt}\right)^+\right]_p^n (1-\alpha_{nc})_p^n \Delta t}{1 - B_{l_p}^n \Delta t \left[\left(\frac{D\alpha_v}{Dt}\right)^- - \left(\frac{D\alpha_v}{Dt}\right)^+\right]_p^n} \tag{37}$$

Multiple calculations of the system of equations (33), with updated values of the phase fractions, are performed to favor a bounded and more accurate solution. This procedure is repeated iteratively until the global conservation of the void fractions is reached. It is important to note that, similarly to what is done in the calculation of the specie transport, the last phase (non-condensable gases in the present work) is usually solved as the complement to reach the unity. In the case of cavitating flows, as discussed in the previous paragraph, the solution of the phase fraction equations is required for closure; this means that, after the iterative procedure just described to calculate independently $\alpha_l$, $\alpha_v$ and $\alpha_{nc}$ is completed, the (small) residual error must be added to the non-condensable phase fraction before the pressure-velocity coupling is calculated.

## 8. Discretization of the convective fluxes in the phase fraction equations (MULES)

The implemented system of phase-fraction equations for the three-phase VOF, Eq. (12), have been discretized following the Multidimensional Universal Limiter with Explicit Solution (MULES), to ensure boundedness and consistency even in presence of flow cavitation and condensation. The method to solve the phase fraction equations is fundamentally explicit and introduces a strict Courant number limit with a direct impact on time step advancement; time step sub-cycling, commonly used to enlarge time-steps in VOF solvers, is applied here to ensure consistency and boundedness of the solution with strong cavitation/condensation. One of the critical issues with the VOF method used is the discretization of the advective term in Eq. (37), that includes either the convective fluxes and the counter-gradient term (compressive fluxes):

$$\sum_f F_{i,f}^n = \sum_f \underbrace{\alpha_{i_f}^n \mathbf{U}_f \cdot \mathbf{S}_f}_{\text{convective fluxes}} + \sum_f \underbrace{\alpha_{i_f}^n \sum_{j \neq i} \alpha_{j_f}^n \mathbf{U}_{C_{ij_f}} \cdot \mathbf{S}_f}_{\text{counter-gradient transport}} = \sum_f F_{\alpha_f}^n + \sum_f F_{C_f}^n \tag{38}$$

Numerical diffusivity of first order schemes might smear the interface; on the other hand, higher order schemes are unstable and may cause numerical oscillations. It is therefore needed to derive advection schemes able to keep the interface sharp and to produce monotonic profiles of the color function. In the modified system of phase fraction equations (33), the Flux Correct Transport (FCT) technique has been applied: flux limiters are computed by an iterative procedure which allows the use of high-order schemes preserving boundedness, mass conservation and sharp interface capturing. The theory originally formulated in [111] was further extended to multi-dimensional problems in [112]. The method involves several stages of calculation: first, the discretization of the advective term $F_{\alpha_f}^n$ is provided by a higher $F_{f,i}^H$ and a lower order $F_{f,i}^L$ (obtained applying a monotonic and a diffusive advective scheme) flux approximation; Then, an anti-diffusive flux ($F_A$) is defined to attempt and reduce the numerical diffusion resulting from the lower order scheme. An estimate of the anti-diffusive fluxes $F^A$ for the $i$-th phase equation is given by:

$$F_{f,i}^A = F_{f,i}^H - F_{f,i}^L \tag{39}$$

Anti-diffusive fluxes $F_{f,i}^A$ are limited to $F_{f,i}^C$ by a flux-limiting technique [112] based on the calculation of a TVD limiter $\lambda$ to prevent undershoots and overshoots in the phase fraction in the control volume:

$$F_{f,i}^C = \lambda\, F_{f,i}^A \quad \text{with} \quad \lambda \in [0,1] \tag{40}$$

being $\lambda = f(F_{\alpha_f}^n)$ a function of the void fractions.

## 9. Definition of test cases and setup

Simulations have been performed on three different cases, in order to test the numerical properties of the newly implemented solver (in the following referred as `interPhaseChangeMixingFoam`) in terms of ability to: a) capture the interfaces, while maintaining them sharp; b) preserve the conservativeness and the boundedness of the solution of the phase-fraction equations with phase-change. Finally, the robustness of the solver and its application to the description of real flow physics is tested on a large parallel simulation of an injector geometry. Validation test cases that will be discussed in the further sections are:

1) the evolution of a two-dimensional bubble rising in a liquid column [50], to test the ability of the solver to properly capture the interface between fluids of different densities;
2) the study of the evolution of a free-surface in a partially cavitating/condensing liquid column, to verify the conservativeness and boundedness while phase-fraction equations are solved with phase-change;
3) a cavitating flow evolving inside an injector nozzle [52,113].

## 10. Bubble rising in a liquid column

The two-dimensional bubble rising in a liquid column [50] has been proposed as a validation test-case to study the ability of the multiphase solvers to capture an interface. The first test case studied consists of a two-dimensional rising bubble problem, where a gas bubble immersed in a chamber filled with liquid moves until it breaks up. The case setup, the boundary conditions and the physical properties of the fluid are described in Fig. 2. Forces acting on the bubble are surface tension and gravity. The domain has an aspect ratio width/height = 0.5; no-slip boundary conditions on the velocity are set at the upper and lower boundaries, while free-slip is applied at the right and left bounds; gravity $\mathbf{g}$ is oriented towards the negative $y$ direction. At time $t = 0$ s, the bubble center is located at $(x, y) = (0.5, 0.5)$ and the bubble radius is $r_{b,0} = 0.25$ m. This test-case has been already used by the authors in [114] to validate a 2-phase VOF solver and it is now used again with some necessary modifications in the case setup: as shown in Fig. 2, the evolution of the bubble in the surrounding liquid (identified by the void fraction $\alpha_1$) is now captured by the transport of two identical phases ($\alpha_2 = \alpha_3$). In this test, phase change is disabled. It is expected that the solution of the three-phase solver tends to the solution of the two-phase solver of [114]. This is not trivial in the VOF framework, since global conservation of the phase fractions is more difficult as the number of phases increases and in a single-fluid solver it is strictly linked to the calculation of the fluid properties (see Eqs. (3) and (4)).

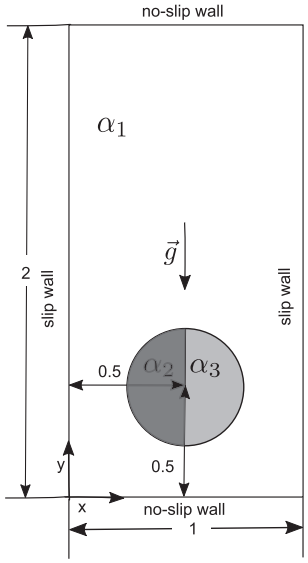


| Parameter | Value | Unit |
|---|---|---|
| $\rho_1$ | 1000 | kg/m$^3$ |
| $\rho_2 = \rho_3$ | 1 | kg/m$^3$ |
| $\mu_1$ | 10 | kg m$^{-1}$ s$^{-1}$ |
| $\mu_2 = \mu_3$ | 0.1 | kg m$^{-1}$ s$^{-1}$ |
| $\mathbf{g}$ | −0.98 | m/s$^2$ |
| $\sigma$ | 1.96 | N/m |
| Re | 35 | – |
| Eo | 125 | – |

**Fig. 2.** Bubble rising in a liquid column: case setup, boundary and initial conditions. Four different grid resolutions are tested: a) 40 × 80 cells; b) 80 × 160 cells; c) 160 × 320 cells; d) 320 × 640 cells (reference solution).

The physical properties of interest of the fluid, listed in Fig. 2, are:

– the Eötvös number Eo, defined as the ratio between the buoyancy force and surface tension:

$$\mathrm{Eo} = \frac{\rho_1 U_g^2 L}{\sigma} \tag{41}$$

– the Reynolds number Re of the liquid, defined as:

$$\mathrm{Re} = \frac{\rho_1 U_g L}{\mu_1} \tag{42}$$

where $L = 2 r_{b,0}$ is the characteristic length scale and $U_g = \sqrt{2 g r_{b,0}}$ is the characteristic rising velocity. At high values of Eo, the bubble shape will be something in between the shape observed for the skirted and the dimpled ellipsoidal-cap regimes, implying that a breakup is likely to occur [115]. Simulations at high values of Eo are challenging for interface capturing

algorithms and can yield to different predictions of the evolution and of the formation of newly created droplets. Following the work of [50], the evolution of the bubble has been investigated for a total time $T = L/U_g$ and a fixed time step with $\Delta t = 1/(2N_x)$ s has been used for time marching. In the surrounding region of the bubble initial conditions for the void fractions are $\alpha_2 = \alpha_3 = 0$ and $\alpha_1 = 1$; in the bubble region, $\alpha_1 = 0$, $\alpha_2 = 1$ and $\alpha_3 = 0$ (left half) and $\alpha_2 = 0$ and $\alpha_3 = 1$ (right half) are set. This leads to a stair-cased shaped interface, so a preliminary simulation without gravity ($\mathbf{g} = 0$) is needed to obtain a smooth initial bubble shape. The results from the zero-gravity precursor simulation are then used as the initial condition for the actual simulation.

Quantitative validation of the described code extensions, based on geometrical metrics proposed in [50], is now presented. For a fair comparison with [50], the grid used is Cartesian with a resolution $N_x \times 2N_x$ cells, being $N_x$ 40, 80, 160 and 320 respectively (four grids were tested in total). The monitored quantities from the simulations were:

a) *bubble center of mass*:

$$\mathbf{x}_c = \frac{\iint_A (\alpha_2 + \alpha_3)\mathbf{x}_c \, \mathrm{d}x\mathrm{d}y}{\iint_A (\alpha_2 + \alpha_3) \, \mathrm{d}x\mathrm{d}y} \tag{43}$$

b) *degree of circularity* for a two-dimensional domain [116], being bubble Area defined as $A_b = \pi r_{eq}^2$:

$$\begin{aligned} C &= \frac{\text{perimeter of equivalent circle}}{\text{actual perimeter of the bubble}} = \frac{2\pi r_{eq}}{\iint_A (\nabla\alpha_2 + \nabla\alpha_3) dxdy} \\ &= \frac{2\pi\sqrt{\frac{A_b}{\pi}}}{\iint_A (\nabla\alpha_2 + \nabla\alpha_3) dxdy} = \frac{2\pi\sqrt{\frac{A_b}{\pi}}}{\iint_A (\nabla\alpha_2 + \nabla\alpha_3) dxdy} \end{aligned} \tag{44}$$

where $r_{eq}$ is the equivalent radius, defined as:

$$r_{eq} = \sqrt{\frac{A_b}{\pi}} = \sqrt{\frac{\iint_A (\alpha_2 + \alpha_3) dxdy}{\pi}} \tag{45}$$

The $C$ parameter is equal to unity for a perfectly circular bubble and lower than unity for other cases;

c) *mean rising velocity*:

$$\mathbf{u}_c = \frac{\iint_A (\alpha_2 + \alpha_3)\mathbf{U} \, \mathrm{d}x\mathrm{d}y}{\iint_A (\alpha_2 + \alpha_3) \, \mathrm{d}x\mathrm{d}y} \tag{46}$$

Results in this section are organized as follows: using the procedure of [50], simulations on the four grids (40 × 80, 80 × 160, 160 × 320 and 320 × 640 cells respectively) are presented, to monitor the grid-dependency of the results. In a second step, the solution from the finest grid is taken as reference solution and it is compared with CFD simulations from three incompressible interfacial flow codes, namely: a) TP2D [117,118] and FreeLIFE [119], that are based on the level-set approach applied on a static grid; b) MooNMD [120] where the interface is tracked in a Lagrangian manner and inner mesh points are then projected onto the interface by solving a linear elasticity problem. The evolution in time of the quantities described above is studied on four grids of different resolution: results are reported in Fig. 3 and in Table 1, while in Figs. 4 and 5 the graphical evolution of the bubble with different grids is reported. Bubble circularity (Fig. 3b) shows a monotonic diminishing tendency, that does not seem very influenced by the mesh resolution, until the beginning of the bubble break-up. Conversely, mean bubble rising velocity (Fig. 3c) does not present a monotonic tendency and this can be justified by the local deformation of the bubble, that is increasing in time. Two local maxima are clearly visible: while the bubble is rising, its velocity reaches a first maximum $\mathbf{u}_{c_{max,1}}$, whose position looks independent by the mesh resolution

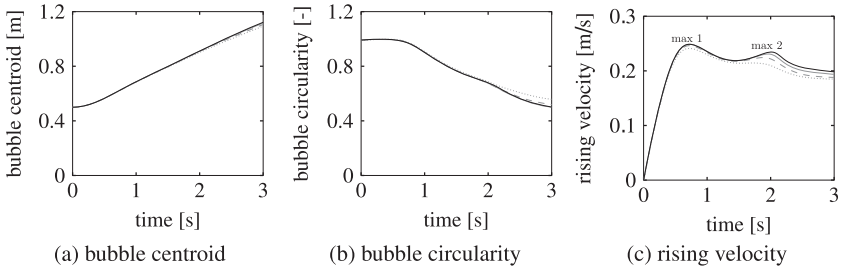


(a) bubble centroid (b) bubble circularity (c) rising velocity

**Fig. 3.** Two-dimensional bubble rising in a liquid column, validation test case. Evolution in time of: (a) bubble centroid location $C$; (b) bubble circularity $C \in [0; 1]$ and (c) bubble rising velocity $\mathbf{u}_c$; circularity is equal to unity if the bubble shape is a perfect circle. Tests have been performed by `interPhaseChangeMixingFoam` using four different grids: .... 40 × 80 cells; – – – 80 × 160 cells; — 160 × 320 cells; ▬ 320 × 640 cells.

**Table 1**
Minimum circularity, maximum rising velocities and final position of center of mass and their corresponding time occurrence for `interPhaseChangeMixingFoam`. $\mathbf{u}_{c_{max,1}}$ and $\mathbf{u}_{c_{max,2}}$ denote the first and the second local peak of the bubble rising velocity, see Fig. 3c.

| Grid | 40 × 80 | 80 × 160 | 160 × 320 | 320 × 640 |
|---|---|---|---|---|
| $C_{min}$ | 0.5579 | 0.5186 | 0.5002 | 0.50072 |
| $t(C_{min})$ | 3.0 | 3.0 | 3.0 | 3.0 |
| $\mathbf{u}_{c_{max,1}}$ | 0.2409 | 0.2461 | 0.2487 | 0.2488 |
| $t(\mathbf{u}_{c_{max,1}})$ | 0.725 | 0.725 | 0.725 | 0.7234 |
| $\mathbf{u}_{c_{max,2}}$ | 0.2144 | 0.2244 | 0.2309 | 0.2345 |
| $t(\mathbf{u}_{c_{max,2}})$ | 1.725 | 1.88125 | 1.959375 | 2.009375 |
| $\mathbf{x}_c(t_{final})$ | 1.094 | 1.1058 | 1.1164 | 1.1223 |

used; this allows to assume that all the grids have sufficient resolution to describe the main features of the bubble before break-up. The second maximum is instead occurring when the tail in the bottom region of the bubble becomes relevant; in this case, the mesh resolution influences the predictions, since the bubble tail and its ligaments are differently described from coarser to finer grid resolution. Thinner predicted tails favor a larger velocity in the second local peak and its shifting to later times. As the break-up of the tail occurs, the mean rising velocity decreases again. Finally, the evolution of the bubble centroid, Eq. (43), is mostly independent by mesh resolution until the size of the tails becomes relevant and influences the position of the bubble mass in the domain.

The evolution of the bubble shape is monitored at different times; the bubble interface is obtained by an iso-contour plot of the liquid void fraction using $\alpha_l = 0.5$ as threshold value. In Fig. 4, the temporal evolution of the bubble using four different meshes is reported to justify previous considerations. From 0 s to 1.8 s the capture of the bubble surface is almost independent by the mesh resolutions used. As soon as the onset of breakup occurs, the grid starts producing different deformations of the elongated filaments (2.2 s) leading to completely different flow configurations, as evidenced in Fig. 5. While coarse grids (40 × 80 and 80 × 160) do not capture any breakup, this starts to appear with the 160 × 320 mesh and it is reproduced with good detail by the finest mesh.

Similarly to [50], relative error of the norm of the temporal evolution of the bubble center of mass $\mathbf{x}_c$, of the bubble circularity C and of the mean rising velocity $\mathbf{u}_c$ are calculated using a suitable reference solution, represented by the finer grid:

$$e_{l_1} = \frac{\sum_{t=1}^{N} |q_{t,ref} - q_t|}{\sum_{t=1}^{N} |q_{t,ref}|} \tag{47}$$

$$e_{l_2} = \left( \frac{\sum_{t=1}^{N} |q_{t,ref} - q_t|^2}{\sum_{t=1}^{N} |q_{t,ref}|^2} \right)^{1/2} \tag{48}$$

$$e_{l_\infty} = \frac{max_t |q_{t,ref} - q_t|}{max_t |q_{t,ref}|} \tag{49}$$

where $q_t$ is the temporal evolution of quantity $q$, and $N$ the number of samples in time of $q$. Standard linear interpolation has been used in order to account for different sampling rates between $q_{t,ref}$ and $q_t$, that are calculated on different grids. For each relative error norm, the Rate Of Convergence (ROC) of $q$ is:

$$ROC \approx \frac{log_{10}(\|e^{k+1}\|/|e^k|)}{log_{10}(h^{k+1}/h^k)} \tag{50}$$

where $k$ denotes the grid refinement level and $h = 1/\Delta x$. Since the finest grid (320 × 640 cells) has been used as reference solution, the computed ROC will not indicate how well a method converges to the exact solution, but how it converges to an approximate solution. In Table 2 the relative error norms and the rates of convergence are reported: more than a linear convergence order is achieved in the $l_1$, $l_2$ and $l_\infty$ norms as the resolution of the grid increases. While the order of convergence for the bubble centroid and for mean rising velocity increases with the grid resolution, the same tendency is not noticed in $l_1$ and $l_2$ norms of the bubble circularity: this is probably due to the fact that the two coarser grids do not exhibit break-up of ligaments. The order of convergence of the $l_\infty$ norm of the bubble circularity increases with the mesh resolution, because its definition is based on the highest absolute deviation between the coarsest and finest mesh: in other words, moments in time characterized by the highest deviations (e.g. bubble break-up) are converging faster with respect to the moments where the bubble is only deformed and where the mesh resolution does not play a significant role.

Finally, a second investigation has been carried out to compare the results from the implemented solver against [50]. The time $t = 3$ s (Fig. 6) is chosen for comparison being the most representative of the bubble breakup. From Fig. 6 it is apparent that the upper part of the bubble is well described by the different solvers, that make use of different methods to transport the interface. Differences can be noticed in the tails produced in the bottom part of the bubble, where each solver differently describes the breakup process, by describing different filament lengths.

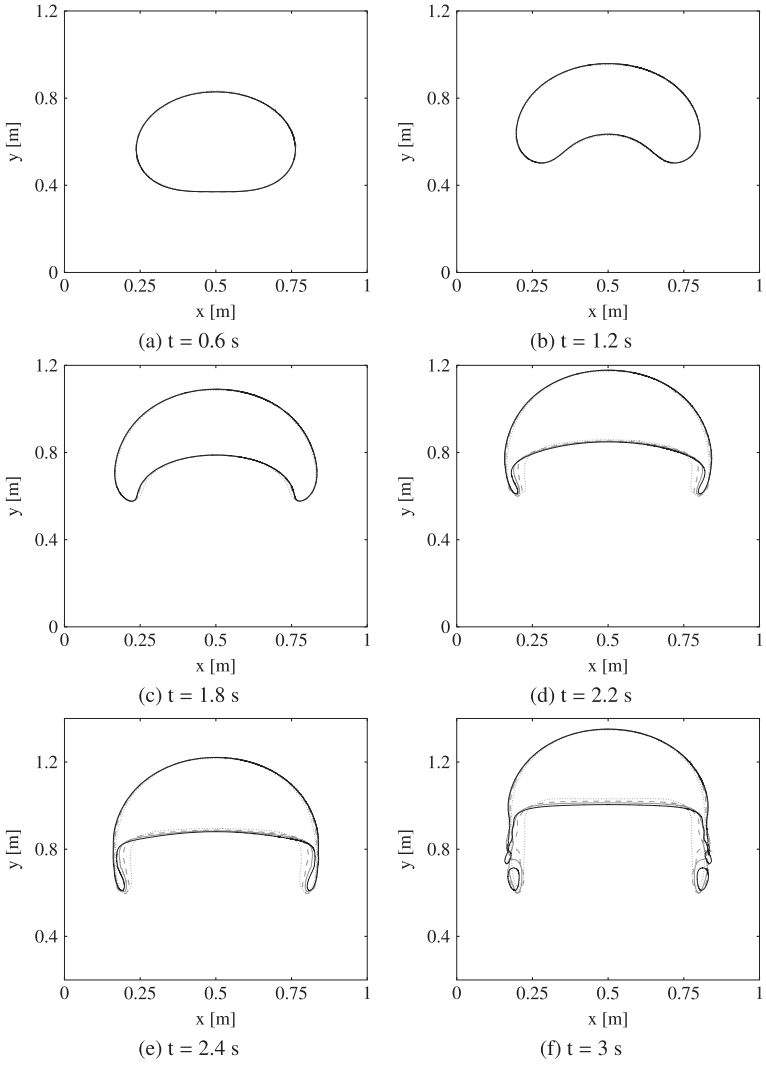


**Fig. 4.** Bubble evolution from 0.6 to 3 s calculated by `interPhaseChangeMixingFoam` on four different grids: .... 40 × 80 cells; – – – 80 × 160 cells; — 160 × 320 cells; ▬ 320 × 640 cells.

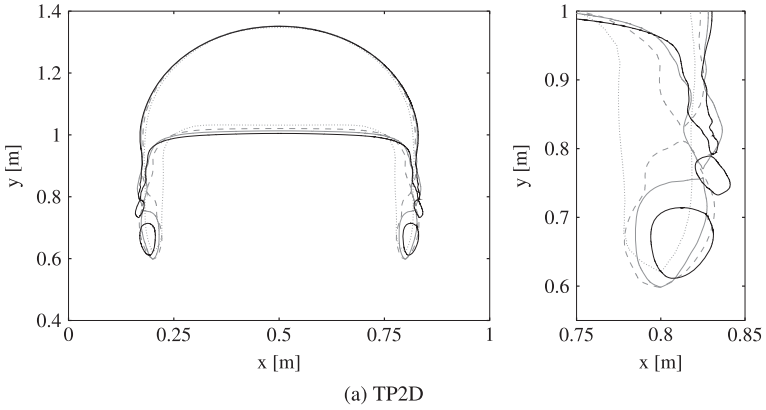


**Fig. 5.** Bubble breakup at time $t = 3$ s. Comparison of `interPhaseChangeMixingFoam` behavior using four different discretizations: .... 40 × 80 cells; – – – 80 × 160 cells; — 160 × 320 cells; ▬ 320 × 640 cells.

**Table 2**
Relative error norms and rates of convergence for different grid resolutions. Results for the grid 320 × 640 is taken as reference.

| | Grid | $e_{l_1}$ % | $ROC_1$ | $e_{l_2}$ % | $ROC_2$ | $\|e\|_{l_\infty}$ % | $ROC_\infty$ |
|---|---|---|---|---|---|---|---|
| $\mathbf{x}_c$ | 40 × 80 | 5.31 | – | 0.66 | – | 10.87 | – |
| | 80 × 160 | 2.85 | 0.8988 | 0.4 | 0.7384 | 6.3 | 0.7865 |
| | 160 × 320 | 1.01 | 1.4986 | 0.17 | 1.2568 | 2.67 | 1.2430 |
| $C$ | 40 × 80 | 2.16 | – | 0.09 | – | 5.74 | – |
| | 80 × 160 | 0.57 | 1.9271 | 0.02 | 1.940 | 1.79 | 1.6779 |
| | 160 × 320 | 0.2 | 1.5213 | 0.008 | 1.5179 | 0.55 | 1.7119 |
| $\mathbf{u}_c$ | 40 × 80 | 1.15 | – | 0.043 | – | 2.54 | – |
| | 80 × 160 | 0.54 | 1.1010 | 0.02 | 0.9669 | 1.47 | 0.7868 |
| | 160 × 320 | 0.14 | 1.9202 | 0.007 | 1.6625 | 0.52 | 1.4966 |

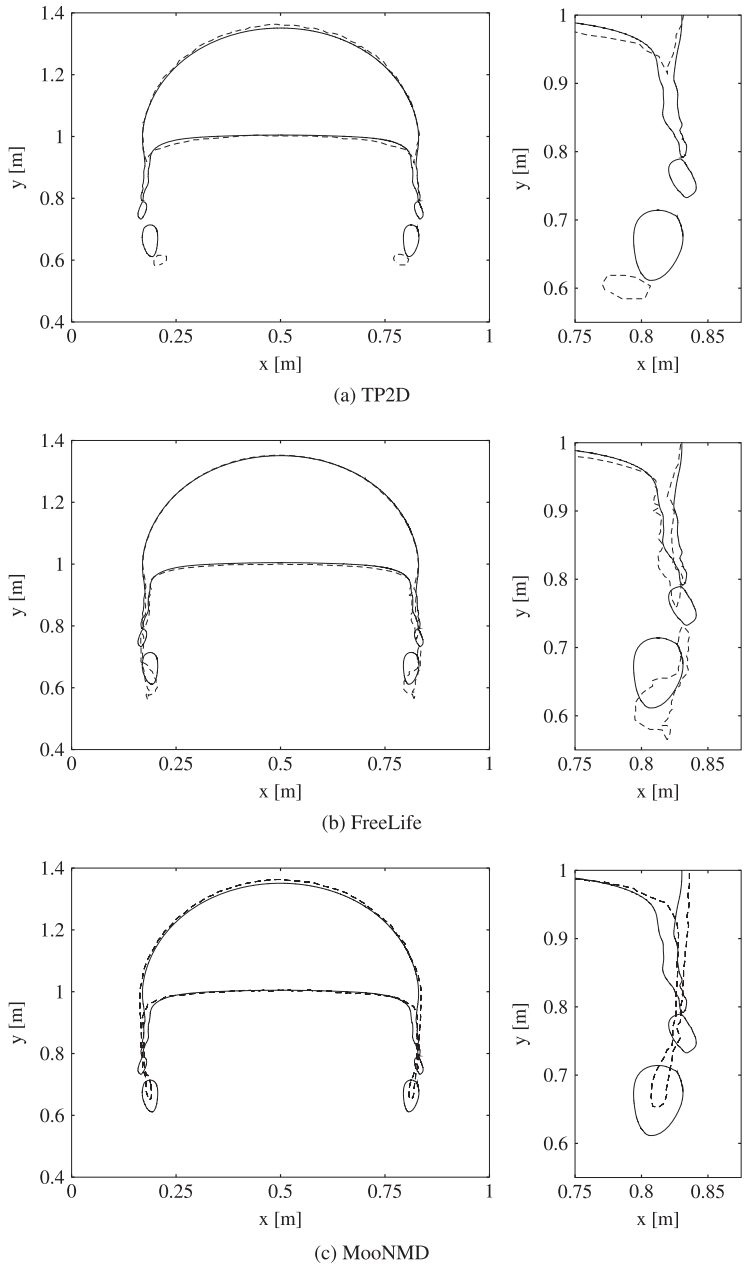


**Fig. 6.** Bubble breakup at time $t = 3$ s; comparison between — `interPhaseChangeMixingFoam` and – – –: (a) TP2D, (b) FreeLife, (c) MooNMD.

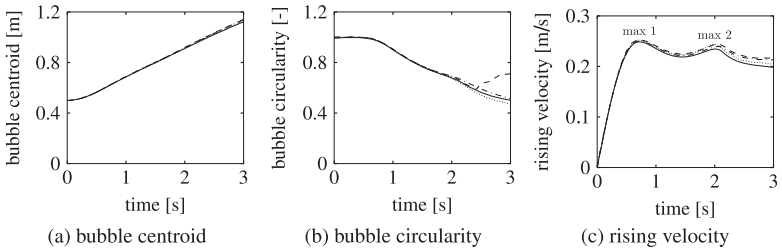


(a) bubble centroid (b) bubble circularity (c) rising velocity

**Fig. 7.** Two-dimensional rising bubble problem, validation test case. Evolution in time of: (a) bubble centroid location $C$; (b) bubble circularity $C \in [0; 1]$ and (c) bubble rising velocity $\mathbf{u}_c$; circularity is equal to unity if the bubble shape is a perfect circle. Legend: — `interPhaseChangeMixingFoam`, – – – TP2D code, — · — FreeLIFE code, ··· MooNMD [50].

**Table 3**
Comparison of: a) minimum bubble circularity, b) maximum rising velocity, c) position of the center of mass for the different codes compared. The grid resolution used for the tests was 320 × 640 cells. Subscripts 1 and 2 denote the first and the second local maximum respectively.

| | `interPhaseChangeMixingFoam` | TP2D | FreeLife | MoonNMD |
|---|---|---|---|---|
| $C_{min}$ | 0.50072 | 0.5943 | 0.4647 | 0.5144 |
| $t(C_{min})$ | 3.0 | 2.3439 | 3.0 | 3.0 |
| $\mathbf{u}_{c_{max,1}}$ | 0.2488 | 0.2538 | 0.2514 | 0.2502 |
| $t(\mathbf{u}_{c_{max,1}})$ | 0.7234 | 0.7340 | 0.7281 | 0.7317 |
| $\mathbf{u}_{c_{max,2}}$ | 0.2345 | 0.2467 | 0.2440 | 0.2393 |
| $t(\mathbf{u}_{c_{max,2}})$ | 2.009375 | 2.0553 | 1.9844 | 2.0600 |
| $\mathbf{x}_c(t_{final})$ | 1.1223 | 1.1387 | 1.1249 | 1.1376 |

However, when analyzing monitoring quantities among different solvers using the same mesh resolution, it is possible to determine if their trends are well reproduced among different approaches (Fig. 7, Table 3).

## 11. Evolution of the free-surface in a partially cavitating/condensating liquid column

In the bubble rising problem, no phase-change is involved. At the time this paper is written, no simple numerical test cases are proposed to check if boundedness and conservativeness is ensured while phase-change occurs in a solver using a VOF method to capture the interface. Mass conservation is easier to achieve with the Homogeneous Equilibrium Model (HEM), the Homogeneous Relaxation Model (HRM) [121–123] and the Bubble Model, but it is critical in VOF methods where phase-change is implemented in the phase-fraction equations. Comparisons between the Bubble Model and the HRM for an injector test case [124] are reported in [125], where it is shown similar behavior in the prediction of the cavitation onset and similar limits in the description of condensation effects. With multiphase flows, the common way to validate models is through visual comparison of the flow evolution: this is still possible when cloud and wake cavitation occur in proximity of the blades, because pockets of vapor are in a large and well defined region near the trailing edge. On the other hand, visualization of bubbly flows inside a nozzle is very hard, because of its micrometric size and of the short lifetime of the vapor bubbles (the order of magnitude is 1 µs). Besides, in both types of cavitating flows it is hard to split the errors coming from the solution of the momentum equation and those coming from the resolution of the phase-fraction equations.

In this work, a simple benchmark configuration is proposed to check boundedness and conservativeness of the VOF solver. The test-case consists of a one-dimensional column, opened at its top, whose dimension is L in y-direction; half of the volume of the column is filled by 95% of liquid and 5% of fuel vapor, while the remaining half of the volume is filled by non-condensable gases (Fig. 8). The system is initially at rest; The pressure distribution over the vertical y-axis is hydrostatic. In a first stage of the test, which duration of 0.1 s, the condensation term is disabled and the saturation pressure of the liquid is set to $p_{sat} = 100300$ Pa; as a consequence, in the regions where the hydrostatic pressure is lower than the saturation pressure, the liquid cavitates, and non-condensable gases are pushed out of the outlet boundary. The final state of the system at $t = 0.1$ s is then used as initial condition for a second stage of the test (from $t = 0.1$ s to $t = 0.2$ s), where the vapor is forced to condensate, by setting the saturation pressure of the fluid to $p_{sat} = 99700$ Pa. The different values of the saturation pressure have been chosen to reproduce similar pressure gradients in the liquid and in the vapor and thus to have similar magnitude of the source terms (with different signs) during cavitation and condensation. In the simulations, no-slip boundary conditions are applied at the lower boundary, free-slip is imposed on the side walls while a Neumann condition is applied at the upper boundary. Tests on two different one-dimensional grid domains have been performed; discretization along the y-axis was respectively made of 1 × 640 cells (this grid will be referred in the following as grid A) and 1 × 1280 cells (grid B). Monitored benchmark quantities are the position of the interface, its sharpness and its velocity, together with the overall mass conservation and the instantaneous mass balance between the liquid fuel and the fuel vapor. The same test-case has been simulated in two dimensions; additional information about the setup together with the analysis of the results are included in Appendix C.

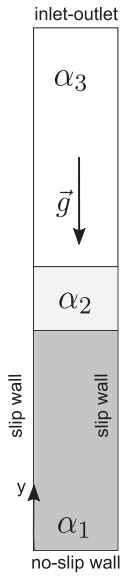


| Initial condition | | |
|---|---|---|
| Parameter | Cavitation case | Condensation case |
| $\alpha_1$ | $\alpha_1(t_0) = 1,\ y \in [0, 0.95)$ | $\alpha_1(t_0) = \alpha_1(t_f)_{cav.}$ |
| $\alpha_2$ | $\alpha_2(t_0) = 1,\ y \in [0.95, 1)$ | $\alpha_2(t_0) = \alpha_2(t_f)_{cav.}$ |
| $\alpha_3$ | $\alpha_3(t_0) = 1,\ y \in [1, 2]$ | $\alpha_3(t_0) = \alpha_3(t_f)_{cav.}$ |
| $p$ | Hydrostatic pressure | Hydrostatic pressure |
| $U$ | $0\ \mathrm{m\,s^{-1}}$ | $0\ \mathrm{m\,s^{-1}}$ |
| $p_{sat}$ | 100300 Pa | 99700 Pa |

| Fluid properties | | |
|---|---|---|
| Parameter | Value | Unit |
| $\rho_1$ | 1000 | $\mathrm{kg\,m^{-3}}$ |
| $\rho_2 = \rho_3$ | 1 | $\mathrm{kg\,m^{-3}}$ |
| $\mu_1$ | 10 | $\mathrm{kg\,(m\,s)^{-1}}$ |
| $\mu_2 = \mu_3$ | 0.1 | $\mathrm{kg\,(m\,s)^{-1}}$ |
| $\mathbf{g}$ | −0.98 | $\mathrm{m\,s^{-2}}$ |
| $\sigma_{12} = \sigma_{13}$ | 1.96 | $\mathrm{N\,m^{-1}}$ |

**Fig. 8.** Domain, boundary conditions, initial condition and fluids properties of the cavitation/condensation test case.

The final purpose of the proposed benchmark is to establish a reference solution to quantify the conservation error of the solver and it can be interesting for comparison of the performance of different methodologies to model phase-change. The following quantities have been used:

1) evolution of the *mass of each phase*:

$$M_i = \int \alpha_i \rho_i dy \tag{51}$$

2) *liquid/vapor and vapor/air mean surface height*:

$$H_{lv} = \frac{\int \mathbf{y_c} \alpha_l (1-\alpha_l) dy}{\int \alpha_l (1-\alpha_l) dy} \qquad H_{va} = \frac{\int \mathbf{y_c} \alpha_{nc} (1-\alpha_{nc}) dy}{\int \alpha_{nc} (1-\alpha_{nc}) dy} \tag{52}$$

Where $y_c$ represents the $y$ component of cell centers

3) *liquid/vapor and vapor/non-condensable gas (air) mean interface velocity*:

$$\mathbf{u}_{lv} = \frac{\int \mathbf{U} \alpha_l (1-\alpha_l) dy}{\int \alpha_l (1-\alpha_l) dy} \qquad \mathbf{u}_{va} = \frac{\int \mathbf{U} \alpha_{nc} (1-\alpha_{nc}) dy}{\int \alpha_{nc} (1-\alpha_{nc}) dy} \tag{53}$$

As in the computation of height, the surface region is identified by the coexistence of the pair of phases.

4) time evolution of the *relative mass error*, to verify if mass is conserved during phase-change:

$$E_{marching} = \frac{|(M_l(t+1) - M_l(t)) - (M_v(t+1) - M_v(t))|}{M_l(t_0)} \tag{54}$$

This is a sufficient condition for global mass balance to be verified.

5) *global mass relative error*:

$$E_{global} = \frac{|(M_l(t_f) - M_l(t_0)) - (M_v(t_f) - M_v(t_0))|}{M_l(t_0)} \tag{55}$$

where the subscripts 0 and $f$ denote respectively the start and the end of the simulation.

A variable time-step is used in the simulation, to preserve a maximum Courant number $CFL_{max} = 0.1$. Second-order differencing schemes have been applied both for temporal and spatial derivatives.

### *11.1. Cavitation test: results*

Starting from an hydrostatic distribution of pressure in the domain, the liquid starts cavitating (Fig. 9b). Being the vapor lighter than liquid, it moves towards the upper part of the domain and pushes the non-condensable gas (air) outside. In Fig. 9a the mass of air in the domain decreases, while the amount of vapor increases (Fig. 9c).

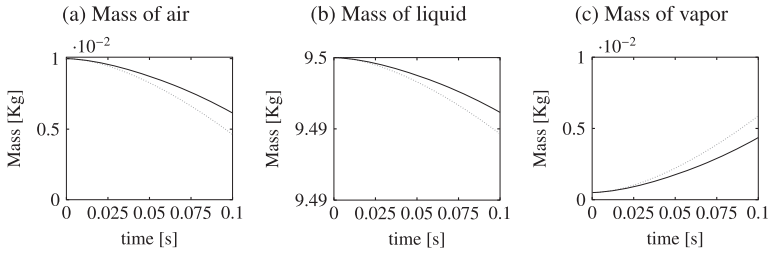


**Fig. 9.** One-dimensional cavitation problem, validation test case. Evolution in time of: (a) air mass; (b) liquid mass; (c) vapor mass. Tests were carried out on two different grids: .... grid A (640 cells); — grid B (1280 cells).

At the end of the simulation the surface height $\Delta y$ of the vapor/air interface is larger if compared to that of the liquid/vapor, as shown in Fig. 10. Being the ratio $\rho_l/\rho_v \simeq 10^3$, the volume of the vapor from the cavitation is larger than the liquid volume.

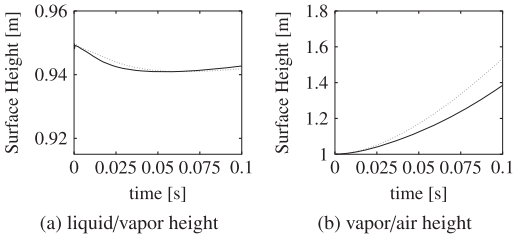


**Fig. 10.** One-dimensional cavitation problem, validation test case. Evolution in time of the surface heights: (a) liquid/vapor, (b) air/vapor on two different grids: .... grid A (640 cells); — grid B (1280 cells).

The evolution of the two surfaces fronts is shown in Fig. 11. In both cases, the interface between the fuel vapor and the non-condensable gas (air) is sharp, because the vapor and the non-condensable gas (air) in the calculation have the same physical properties; this particular condition avoids any instability at the interface that would produce mixing of the fluids and then lead to a diffusion of the interface. Conversely, the liquid/vapor interface is stretched towards the opposite

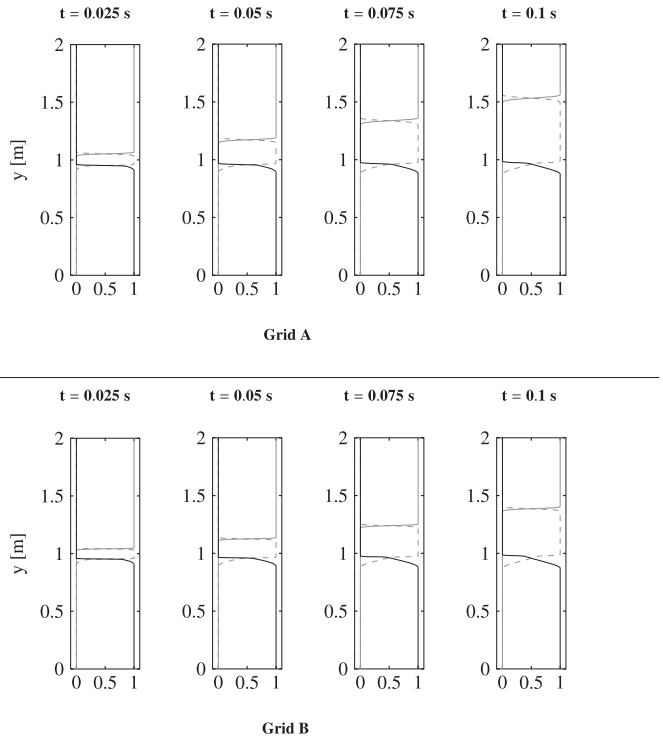


**Fig. 11.** One-dimensional cavitation problem. Evolution of the void fractions from 0.025 to 0.1 s. Top) grid A, 1 × 640 cells; bottom) grid B, 1 × 1280 cells. Legend: $\alpha_l$ —, $\alpha_{nc}$ —, $\alpha_v$ – – –.

direction: vapor moves towards the upper part of the column, while liquid tends to stay at the bottom of the domain because of its higher density.

The liquid/vapor and the air/vapor interface velocities calculated by Eq. (53), are reported in Fig. 12a. The mass of each phase-fraction has then been monitored to compute the time step continuity error and the global conservation error for each phase.

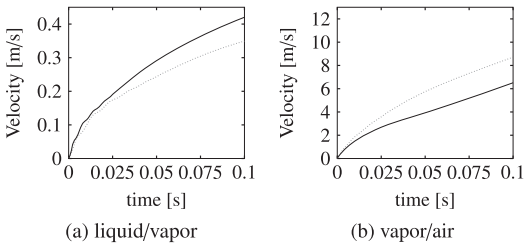


**Fig. 12.** One-dimensional cavitation problem, validation test case. Evolution in time of the mean interface velocity (Eq. (53)): (a) liquid/vapor; (b) vapor/non-condensable gas for two different grids: .... 640 cells; — 1280 cells.

The evolution of the time step continuity error is shown in Fig. 13 on the left. Both for the coarse (grid A) and the fine mesh (grid B), the error is very small. At the beginning of the simulation and in the early time steps (until time = 0.02 s), it shows an increase that is dependent on the initial conditions, but it is then stabilized to a small value. As expected, the continuity error is larger for the coarsest grid than the finest grid, but it is still very small and therefore acceptable. In Fig. 13 the evolution of volume-weighted average void fractions:

$$\overline{\alpha}_i = \sum_{j=1}^{n_c} \frac{\alpha_{i_j} V_j}{V} \tag{56}$$

and the global conservation of the volume-weighted void fractions

$$\overline{\alpha} = \sum_{i=1}^{3} \overline{\alpha}_i \tag{57}$$

are shown. In Eq. (56) and (57), $n_c$ is the number of computational cells, while V is the total volume of the mesh:

$$V = \sum_{j=1}^{n_c} V_j \tag{58}$$

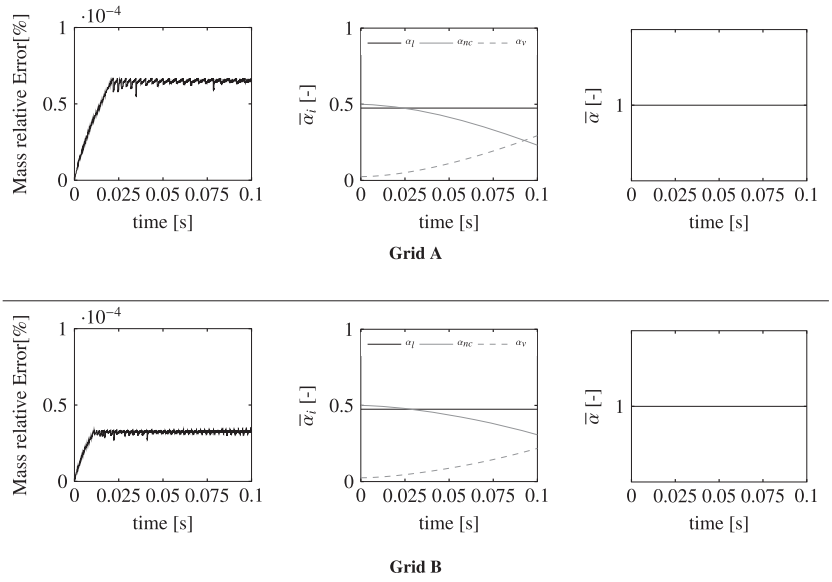


**Fig. 13.** One-dimensional cavitation test case, evolution in time of: left) mass relative error; center) volume-weighted void fractions; right) sum of the volume-weighted void fractions. Grid A: 1 × 640 cells. Grid B: 1 × 1280 cells.

As apparent from Fig. 13, the boundedness and conservativeness of the solution of the void fractions is satisfied. Also, the global mass error (Table 4) proves that mass is properly conserved during the simulation with very limited error peaks.

**Table 4**
Relative error on the global mass conservation for the cavitation test case.

| No. cells | 640 | 1280 |
|---|---|---|
| $E_{global}\%$ | 0.11301 | 0.0811 |

### 11.2. Condensation test

The distribution of the phase-fractions derived from the calculation of the liquid column problem with cavitation is then used as the initial condition for the condensation problem. In Fig. 14b it is shown that as soon as the condensation is artificially triggered (by changing the threshold value of the liquid saturation pressure), the phase fractions of liquid and the vapor start changing: condensation induces negative velocity fluxes at the liquid/vapor interface, and the vapor changes direction of its motion, causing a suction of non-condensable gas (air) from the upper boundary.

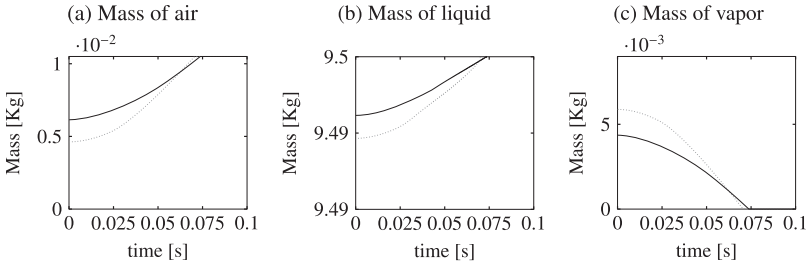


**Fig. 14.** One-dimensional condensation problem, validation test case. Evolution in time of: (a) liquid mass; (b) vapor mass and (c) air mass for two different grids: .... grid A; — grid B.

At $t = 0.075$ s, the condensation is completed; this is confirmed either by the constant value of the surface height (Fig. 15) and by the evolution of the surface (Fig. 16). With condensation, the vapor/air interface is still quite sharp, despite fluctuations at the vapor/liquid interface are visible in Fig. 16 ($t = 0.05$ s); their nature is purely numerical and their existence can be justified by analyzing the implicit and the explicit part of the source term in the discretized form of the void fraction equations, Eq. (33):

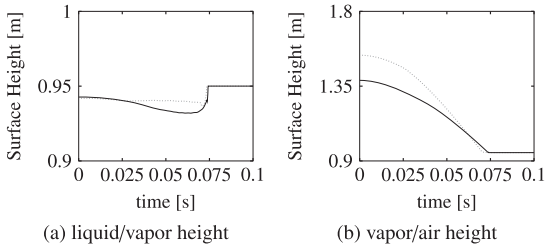


**Fig. 15.** One-dimensional condensation problem, validation test case. Evolution in time of the surface heights: (a) liquid/vapor; (b) air/vapor on two different grids: .... grid A; — grid B.

– when air impacts the liquid surface, the implicit part of the source term in the second equation of (33) reads:

$$B_v^n \left[ \left( \frac{D\alpha_v}{Dt}^+ \right) - \left( \frac{D\alpha_v}{Dt}^- \right) \right]_p \tag{59}$$

during condensation, $(\frac{D\alpha_v}{Dt}^-) = 0$ while $(\frac{D\alpha_v}{Dt}^+) > 0$; from Eq. (25), it follows:

$$\frac{D\alpha_v}{Dt}^+ = f(p - p_{sat}) \tag{60}$$

if fluctuations in pressure appears, then an error peak in Fig. 18 is observed;

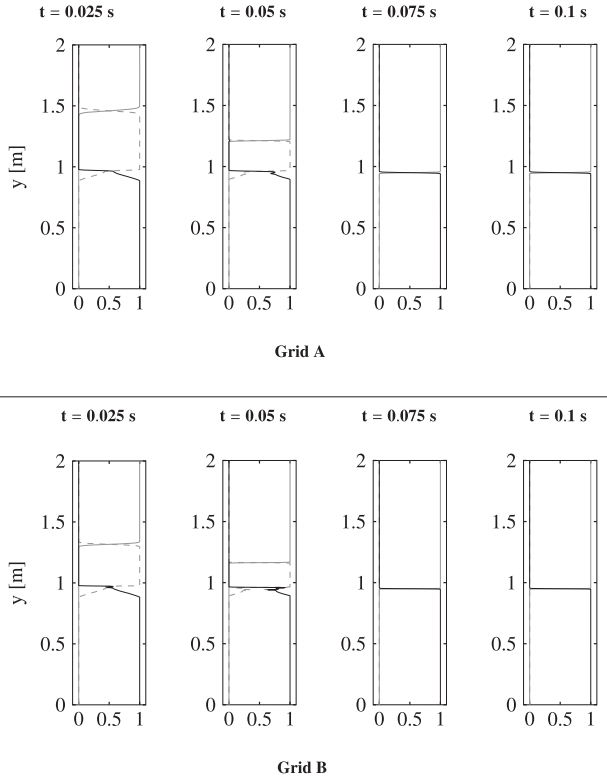


**Fig. 16.** One-dimensional condensation problem. Evolution of the void fractions from 0.025 to 0.1 s. Top) grid A, 1 × 640 cells; bottom) grid B, 1 × 1280 cells. Legend: $\alpha_l$ —, $\alpha_{nc}$ —, $\alpha_v$ – – –.

– the explicit part of the source term in the first equation of (33) is:

$$B_l^n \left( \frac{D\alpha_v}{Dt}^+ \right)_p^n (1-\alpha_{nc})_p^n \tag{61}$$

during condensation, $(\frac{D\alpha_v}{Dt}^+) > 0$, $p > p_{sat}$. By Eqs. (60) and (61), pressure results linked to the evolution of the void fractions.

As shown in Fig. 18, non-conservation of mass is negligible but it is always present: this is a consequence of adding the source terms $S_\alpha$ for phase-change in the projection method as volume fluxes.

With condensation, the liquid/vapor and vapor/non-condensable gas (air) mean interface velocity (Eq. (53)) becomes negative in the $y$ direction and reaches the zero velocity condition in a steep way (see Fig. 17).

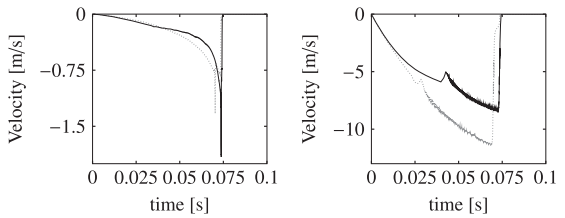


**Fig. 17.** One-dimensional condensation problem, validation test case. Evolution in time of the mean interface velocity (Eq. (53)): (a) liquid/vapor; (b) vapor/non-condensable gas for two different grids: .... 640 cells; — 1280 cells.

Mean interface velocity in Fig. 17 is estimated by Eq. (53). In Fig. 17b, minor fluctuations in the vapor/non-condensable gas mean interface velocity appear. This is a consequence of the numerical algorithm adopted for the iterative solution of Eq. (12), because the residual error at the last iteration is added to $\alpha_{nc}$. The fluctuations in the solution of $\alpha_{nc}$ have a very minor impact on mass conservation (see Fig. 18, $t < 0.07$ s). In Fig. 18, a peak in the error of the mass conservation is

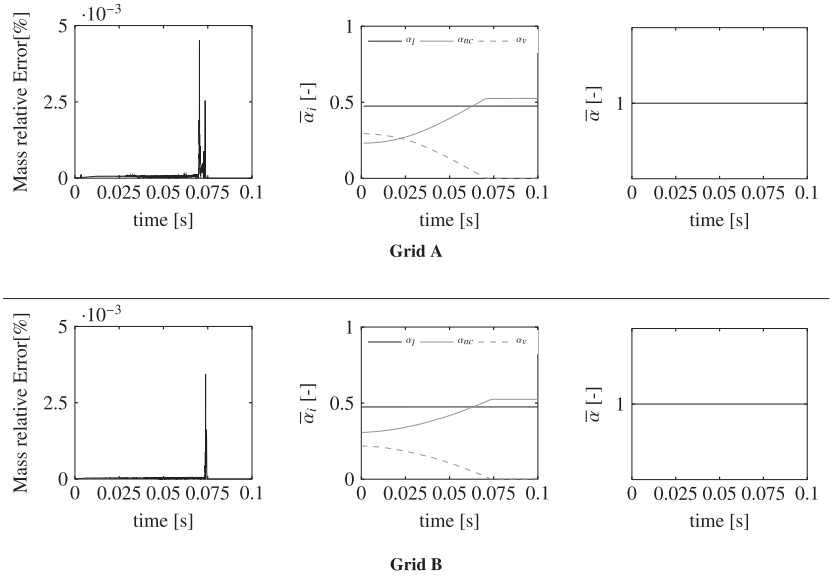


**Fig. 18.** One-dimensional condensation test case, evolution in time of: left) mass relative error; center) volume-weighted void fractions; right) sum of the volume-weighted void fractions. Grid A: 1 × 640 cells. Grid B: 1 × 1280 cells.

centered around $t = 0.075$ s. From the analysis of the variation of volume-weighted void fractions in time, this peak occurs when the vapor fully condenses ($\alpha_v \to 0$) and the number of phases that switches from three to two. As shown in the same figure, the magnitude of the error peaks is very limited (about $4 \cdot 10^{-3}$%) and the mass relative error follows the same trend that has been noticed in the cavitation problem: after a time of about 0.02 s, during which the error grows because of the initialization, the error stabilizes to a value of the order of $10^{-4}$%. Also for condensation, it is then demonstrated that mass conservation is satisfied with a good level of accuracy. Boundedness and conservativeness of the solution of the void fractions (Eqs. (56) and (57)) in the domain is satisfied also here.

Moreover, Fig. 18 shows also that conservation of the void fraction with phase-change is preserved very well during the simulation: the global mass error (Table 5) is very limited with both the grids.

**Table 5**
Relative (percentage) error on global mass conservation for condensation test case.

| No. cells | 640 | 1280 |
|---|---|---|
| $E_{global}$% | 0.1126 | 0.0707 |

## 12. Simulation of internal nozzle flows

The final problem used for the validation is based on the experiments from [52] and [113], that consist of water injection in an air reservoir. The thermodynamic conditions of the fluids are listed in Table 6.

**Table 6**
Thermodynamic properties for $H_2O_{(liq)}$, $H_2O_{(vap)}$, and non-condensable gas (air) at $T = 20\,°C$.

| Parameter | Fluid | | | Unit |
|---|---|---|---|---|
| | $H_2O_{(liq)}$ | $H_2O_{(vap)}$ | Air | |
| Density | 998 | 0.73853 | 1.19 | kg/m$^3$ |
| Dynamic viscosity | $1.2 \cdot 10^{-3}$ | $1.227 \cdot 10^{-5}$ | $1.725 \cdot 10^{-5}$ | kg/(ms) |
| Surface tension | 0.07 | | | N/m |
| Saturation pressure | 2300 | | | Pa |

The transparent injector presents an asymmetric nozzle with a squared-shaped cross-section. A sketch of the nozzle geometry and position of the Laser Doppler Velocimetry (LDV) beams is reported in Fig. 19, while a detailed description of the experimental apparatus is documented in [52] and [39].

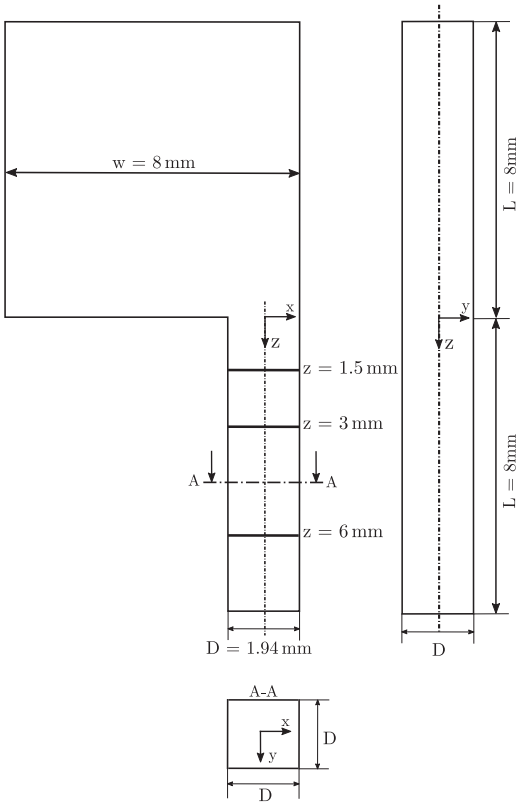


**Fig. 19.** Sketch of injector geometry and locations of LDV measurements.

In the present work, the operating condition with an inlet pressure of 0.22 MPa was simulated and a validation with LDV measurements available from the literature is shown. Input parameters for the simulation are listed in Table 7; the cavitation number (Ca), the liquid Reynolds number ($Re_l$), the Weber number (We) and Ohnesorge number (Oh) are defined as follows:

$$Ca = \frac{p_{amb} - p_{sat}}{0.5\rho_l U_l^2} \tag{62}$$

$$Re_l = \frac{p_l U_l D}{\mu_l} \tag{63}$$

$$We = \frac{\rho_l U_l^2 D}{\sigma} \tag{64}$$

$$Oh = \frac{\sqrt{We}}{Re} \tag{65}$$

where $p_{amb}$ is the ambient pressure, $p_{sat}$ is the saturation pressure of the liquid, $\rho_l$ the density of the liquid water and $U_l$ is the mean liquid velocity computed from Measured volumetric flow rate and nozzle cross-section area.

**Table 7**
Experimental operation condition for 0.22 MPa operative point.

| Parameter | Value | Unit |
|---|---|---|
| $p_{inlet}$ | 0.22 | MPa |
| $p_{amb}$ | 0.1 | MPa |
| Meas. volumetric flow rate $Q$ | $4.8 \cdot 10^{-5}$ | $m^3/s$ |
| Mean liquid velocity $U_l$ | 12.8 | m/s |
| Re | 20577 | – |
| Ca | 1.2 | – |
| We | 4496.3 | – |
| Oh | $3.26 \cdot 10^{-3}$ | – |

According to [126], being $\rho_l/\rho_{air} \sim 10^3$, the regime of the jet flow is in between second wind-induced breakup and the atomization regime; the jet is therefore wavy, as it has also been observed in [52]. The cavitation number suggests the existence of a developing cavitation regime as well, where a vapor cloud forms without reaching the spray domain. The grid used for the simulations is reported in Fig. 20; in order to limit the overall number of grid cells by ensuring a proper resolution for a LES simulation, several refinement regions were selected and a wide use of cell gradings was adopted.

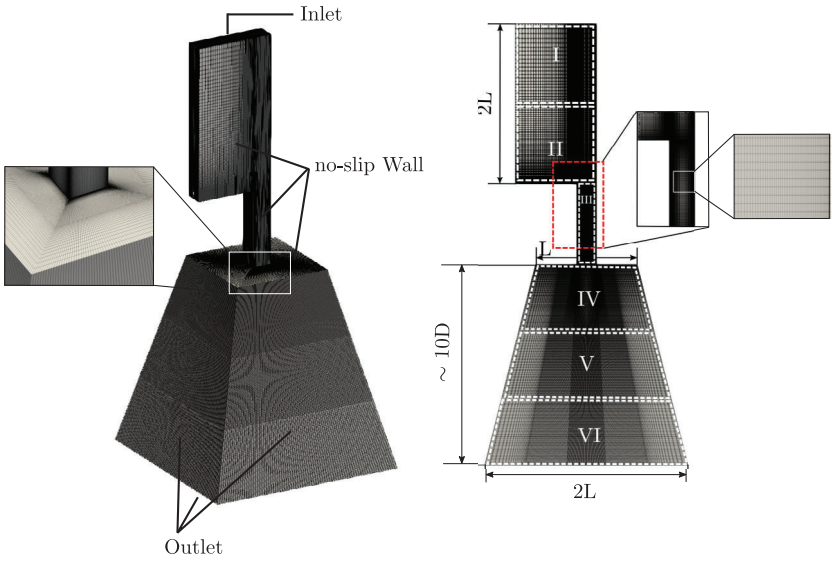


**Fig. 20.** Injector geometry: domain discretization and refinement regions.

Overall information about mesh resolution, cell size and aspect ratio for each region is listed in Table 8.

**Table 8**
Grid resolution and refinement levels for each mesh region.

| Mesh region | Mesh size [µm] | | | No. cells |
|---|---|---|---|---|
| | *x* ratio | *y* ratio | *z* ratio | |
| **I** | 6.5/344 | 6.5/59.8 | 264/490 | 286120 |
| **II** | 6.5/344 | 6.5/59.8 | 26.5/264 | 1020377 |
| **III** | 6.5/59.8 | 6.5/59.8 | 26.5/106 | 1149840 |
| Nozzle refinement block | 3.25/29.9 | 3.25/29.9 | 13.25/53 | 9005544 |
| **IV** | 7.5/443 | 7.5/443 | 27.8/58.3 | 5138880 |
| **V** | 54.6/531 | 54.6/531 | 58.3/85.1 | 2560000 |
| **VI** | 74.1/620 | 74.1/620 | 85.1/117 | 2016000 |
| Domain | | | | $\sim 2.1 \cdot 10^6$ |

In Fig. 20, the spray domain includes twelve refinement regions, four in the radial direction and three in the axial direction. Atmospheric pressure condition is applied on the lateral and bottom surfaces of the spray domain; no-slip wall boundary conditions on velocity are set at the walls. Both the fluids are assumed to be incompressible and isothermal; the numerical models and parameters are listed in Table 9.

**Table 9**
Numerical setup and models parameter.

| Numerical setup | |
|---|---|
| Bubble number density | $10^{15}$ m$^{-3}$ |
| Bubble Nuclei Diameter | 1.5 µm |
| Turbulence Model | LES-WALE [108] |
| $CFL_{max}$ | 0.25 |
| Outer corrector | 7 |
| void fraction corrector | 2 |
| Precursor part | 1.5 ms |
| Averaging part | 0.5 ms |

The averaging procedure on the benchmarked quantities to be compared with LDV measurements and analysis of spray pattern is calculated after 4 m*s* and it lasts 9 m*s*. The numerical setup is the same as discussed in Sec. 7 and Sec. 10. Non-dimensional parameters calculated from the simulation results are in line with the values reported in Table 7. In Fig. 21, a comparison between simulation and experiments is shown; cavitation starts at the left corner, where a recirculation zone makes pressure drops below $P_{sat}$; this is classified as geometry induced cavitation.

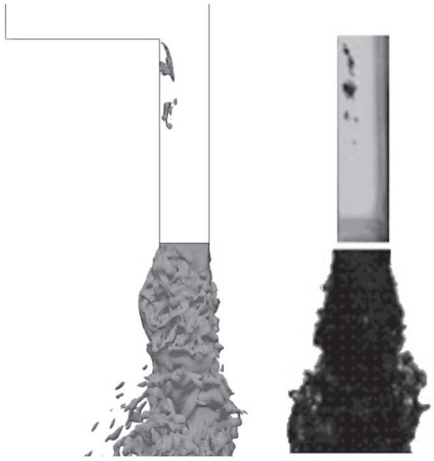

**Fig. 21.** Internal nozzle flow test case [52]. Left) `interPhaseChangeMixingFoam`; right) visualizations from experiments.

The cloud of vapor does not reach the outlet of the nozzle but condensates at about 5 mm from the nozzle inlet. This developing cavitation regime is justified by the small inlet pressure of the experiment and by the high L/D ratio ($L/D \sim 4$); besides, it favors the detachment of fluid at the corner and the formation of a recirculation zone, where a consistent amount of turbulence is produced. In-nozzle turbulence is responsible of the primary breakup of the liquid jet at the nozzle tip, where the aerodynamic forces start triggering surface instabilities. In the specific operating point studied, vapor bubbles are not acting as promoters for the primary breakup since they collapse before reaching the spray domain; this usually happens at higher pressures at the inlet [32,46,52]. Comparisons with experimental profiles of average and rms values of the stream-wise velocity at three different positions inside nozzle from [52] are reported in Fig. 22. Probes were located in the channel center plane ($x = 0$ mm, $y = 0$ mm) at different positions along the nozzle axis: $z = 1.5$ mm, $z = 3$ mm and $z = 6$ mm downstream of the nozzle entrance. In Fig. 22, black filled circles are the experimental sampled points, while time-averaged CFD results are plotted as continuous black solid lines.

The agreement between experiments and predicted average velocity, also when both liquid and vapor are present, looks satisfying. This situation corresponds to negative velocity values ($z = 1.5$ mm, $z = 3$ mm) in the recirculation zone, where a certain amount of vapor is generated due to the pressure drop of the fluid at the nozzle entrance. At $z = 6$ mm, the vapor cloud has already collapsed and the stream-wise velocity assumes only positive values. Also rms values of the velocity are captured fairly well. The small over-prediction of the fluctuating velocity at the left-hand corner of the channel, when vapor and liquid are present at the same time, shows that the amount of predicted turbulent kinetic energy is too large in that region: this could be due to a slight overestimation of vapor production along the shear layer which causes enhancement of the velocity gradients and thus of the turbulence production, as it has already been noticed in [46].

## 13. Conclusions

The aim of the presented study was to illustrate the recently developed three-phase VOF pressure based solver, with the ability to capture the air/vapor interface and model phase-change phenomena as well. Two numerical tests cases and an injector geometry have been used for validation. The first case, the modified rising bubble problem, proved the ability of the implemented three-phase solver to capture the interface with very limited diffusion, providing similar results of high-order solvers. The second numerical problem, proposed for the first time by the authors, was thought to verify mass conservation properties of the VOF solver with phase-change. Both with cavitation and condensation, the solver proved to be able to limit the mass relative error to a very small value with some minor, almost negligible, error peaks of the order of 0.001% when bubbles collapse. Finally, a simulation of an injector geometry has been performed at one operating pressure condition for which LDV measurements inside the injector nozzle were available from the literature; the aim of the simulation was to prove the predictive capability on real internal nozzle-flow conditions. Comparisons with high-speed camera visualization have shown that the cavitation developing regime has been well-captured.

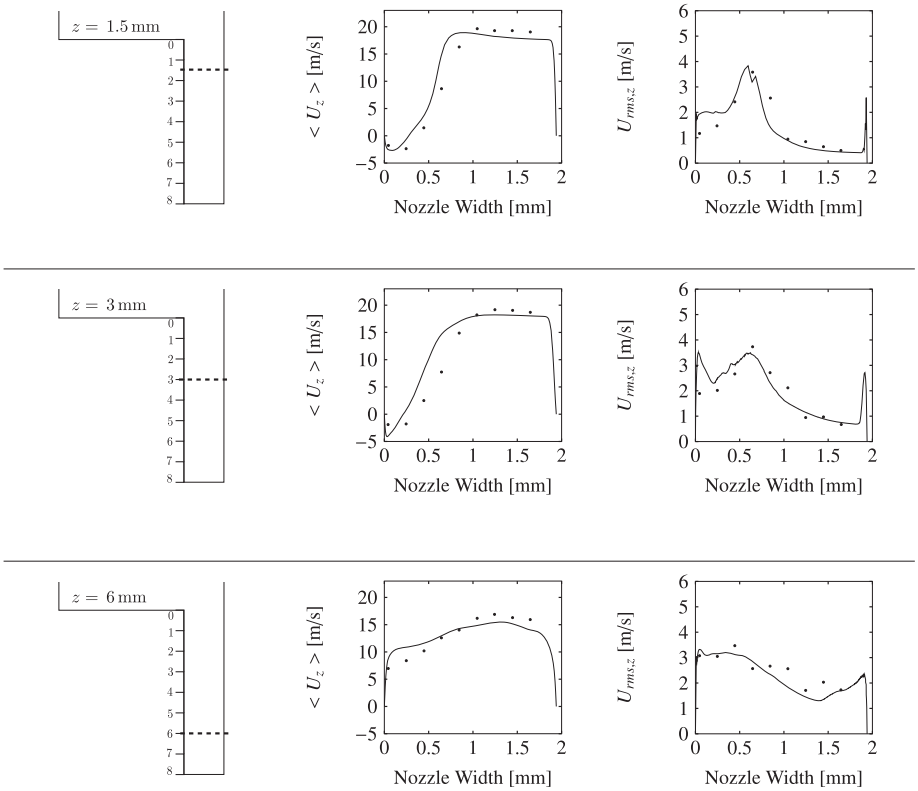


**Fig. 22.** Mean streamwise in-nozzle flow velocity and RMS turbulent velocity at different positions: $z = 1.55$ mm (top), $z = 3$ mm (middle), $z = 6$ mm (bottom); • experiments [52] — `interPhaseChangeMixingFoam`.

## Declaration of competing interest

The authors declare that they have no known competing financial interests or personal relationships that could have appeared to influence the work reported in this paper.

## Acknowledgements

Authors gratefully acknowledge the Laboratory Computing Resource Center (LCRC) at Argonne National Laboratory for the computing resources provided through the `KNL-OPENFOAM-VOF` project. Code implementation has been carried out by the authors and included in a in-house C++ library developed at the Dept. of Aerospace Science and Technology at Politecnico di Milano (PoliMi/DAER), that is compliant with the most recent version of the software OpenFOAM released by the OpenFOAM Foundation [53].

## Appendix A. Derivation of the source terms in a three-phase VOF solver with phase change

In this section, the derivation of the formulation of the term $S_\alpha$ of Eq. (6) is shown. From the definition of total derivative:

$$\frac{D\alpha_i}{Dt} = \frac{\partial \alpha_i}{\partial t} + \mathbf{U} \cdot \nabla \alpha_i \tag{A.1}$$

it follows:

$$\frac{\partial \alpha_i}{\partial t} + \nabla \cdot (\mathbf{U}\alpha_i) = \frac{D\alpha_i}{Dt} + \alpha_i \nabla \cdot \mathbf{U} \tag{A.2}$$

so that system of equations (5) can be written in the equivalent form:

$$\begin{cases} \dfrac{D\alpha_l}{Dt} = -\alpha_l \nabla \cdot \mathbf{U} - \dfrac{S_\alpha}{\rho_l} \\ \dfrac{D\alpha_v}{Dt} = -\alpha_v \nabla \cdot \mathbf{U} + \dfrac{S_\alpha}{\rho_v} \\ \dfrac{D\alpha_{nc}}{Dt} = -\alpha_{nc} \nabla \cdot \mathbf{U} \end{cases} \tag{A.3}$$

where the subscripts *l*, *v* and *nc* are used for liquid, vapor and non-condensable gases respectively. To ensure the boundedness of the solution of (A.3), the derived form of the compatibility condition $\alpha_l + \alpha_v + \alpha_{nc} = 1$ is used for closure:

$$\frac{D\alpha_l}{Dt} + \frac{D\alpha_v}{Dt} + \frac{D\alpha_{nc}}{Dt} = 0 \tag{A.4}$$

Substituting the expressions for $\frac{D\alpha_l}{Dt}$ and $\frac{D\alpha_{nc}}{Dt}$ from (A.3) into Eq. (A.4), the cavitation source term $S_\alpha$ is written as a function of $\frac{D\alpha_v}{Dt}$:

$$S_\alpha = \rho_l(\alpha_l + \alpha_{nc})\, \nabla \cdot \mathbf{U} - \rho_l \frac{D\alpha_v}{Dt} \tag{A.5}$$

Similarly, starting from Eq. (13) and considering each phase as incompressible, it holds:

$$\begin{aligned} \nabla \cdot \mathbf{U} = & -\frac{1}{\rho}\frac{D\rho}{Dt} \\ = & -\frac{1}{\rho}\left[\frac{D(\rho_l\alpha_l)}{Dt} + \frac{D(\rho_{nc}\alpha_{nc})}{Dt} + \frac{D(\rho_v\alpha_v)}{Dt}\right] \\ = & -\frac{1}{\rho}\left(\rho_l\frac{D\alpha_l}{Dt} + \rho_{nc}\frac{D\alpha_{nc}}{Dt} + \rho_v\frac{D\alpha_v}{Dt}\right) \\ = & -\frac{1}{\rho}\left(-\rho_l\alpha_l\nabla\cdot\mathbf{U} - S_\alpha - \rho_{nc}\alpha_{nc}\nabla\cdot\mathbf{U} + \rho_v\frac{D\alpha_v}{Dt}\right) \end{aligned} \tag{A.6}$$

so

$$S_\alpha = \rho_v\frac{D\alpha_v}{Dt} - (\rho_l\alpha_l + \rho_{nc}\alpha_{nc} - \rho)\,\nabla\cdot\mathbf{U} \tag{A.7}$$

From the combination of Eq. (A.5) and Eq. (A.7), the final form of the mass conservation for an incompressible flow, Eq. (13), takes the form:

$$\nabla\cdot\mathbf{U} = \frac{\rho_l - \rho_v}{\rho + \alpha_{nc}(\rho_l - \rho_{nc})}\frac{D\alpha_v}{Dt} \tag{A.8}$$

The formulation of the term $S_\alpha$ is obtained from the transport equation of $\alpha_v$ of (A.3):

$$\frac{D\alpha_v}{Dt} = -\alpha_v\nabla\cdot\mathbf{U} + \frac{S_\alpha}{\rho_v} \tag{A.9}$$

which is rewritten as:

$$S_\alpha = \rho_v\frac{D\alpha_v}{Dt} + \rho_v\alpha_v\nabla\cdot\mathbf{U} \tag{A.10}$$

and:

$$\begin{aligned} S_\alpha &= \rho_v\frac{D\alpha_v}{Dt} + \rho_v\alpha_v\frac{\rho_l - \rho_v}{\rho + \alpha_{nc}(\rho_l - \rho_{nc})}\frac{D\alpha_v}{Dt} \\ &= \rho_v\frac{D\alpha_v}{Dt}\left[1 + \frac{\alpha_v(\rho_l - \rho_v)}{\rho + \alpha_{nc}(\rho_l - \rho_{nc})}\right] \\ &= \rho_v\frac{D\alpha_v}{Dt}\left[\frac{\rho + \alpha_{nc}\rho_l - \alpha_{nc}\rho_{nc} + \alpha_v\rho_l - \alpha_v\rho_v}{\rho + \alpha_{nc}(\rho_l - \rho_{nc})}\right] \\ &= \rho_v\frac{D\alpha_v}{Dt}\left[\frac{(\rho - \alpha_{nc}\rho_{nc} - \alpha_v\rho_v) + \alpha_{nc}\rho_l + \alpha_v\rho_l}{\rho + \alpha_{nc}(\rho_l - \rho_{nc})}\right] \\ &= \rho_v\frac{D\alpha_v}{Dt}\left[\frac{\alpha_l\rho_l + \alpha_{nc}\rho_l + \alpha_v\rho_l}{\rho + \alpha_{nc}(\rho_l - \rho_{nc})}\right] \\ &= \rho_v\frac{D\alpha_v}{Dt}\left[\frac{\rho_l\,(\alpha_l + \alpha_v + \alpha_{nc})}{\rho + \alpha_{nc}(\rho_l - \rho_{nc})}\right] \end{aligned} \tag{A.11}$$

leading to:

$$S_\alpha = \rho_v \frac{D\alpha_v}{Dt}\left[\frac{\rho_l}{\rho + \alpha_{nc}(\rho_l - \rho_{nc})}\right] \tag{A.12}$$

and to the final form of the system (5)

$$\begin{cases} \dfrac{\partial \alpha_l}{\partial t} + \nabla \cdot (\mathbf{U}\alpha_l) = -\dfrac{\rho_v}{\rho + \alpha_{nc}(\rho_l - \rho_{nc})}\dfrac{D\alpha_v}{Dt} \\ \dfrac{\partial \alpha_v}{\partial t} + \nabla \cdot (\mathbf{U}\alpha_v) = \dfrac{\rho_l}{\rho + \alpha_{nc}(\rho_l - \rho_{nc})}\dfrac{D\alpha_v}{Dt} \\ \dfrac{\partial \alpha_{nc}}{\partial t} + \nabla \cdot (\mathbf{U}\alpha_{nc}) = 0 \end{cases} \tag{A.13}$$

## Appendix B. Derivation of the cavitation term for a three-phase VOF solver

The rates of fuel vaporization and condensation are determined by a simplification of the Rayleigh-Plesset equation which assumes spherical bubbles of radius $R$ subject to uniform pressure variations. Spherical bubbles are then represented by a fraction of the vapor phase in the computational cell; from [81] and considering that a in a cell liquid, vapor and air may coexist, it follows:

$$V_v = N_b \frac{4}{3}\pi R^3 = n_0 V_l \frac{4}{3}\pi R^3 \tag{B.1}$$

where $V_v$ and $V_l$ are respectively the volume of the vapor and the liquid in the computational cell of volume V, $N_b$ is the number of spherical bubbles of radius $R$ in the computational cell and $n_0$ is defined as the bubble concentration per unit volume of pure liquid. From Eq. (B.1), it follows:

$$\frac{V_v}{V_l + V_v} = \frac{n_0 V_l \frac{4}{3}\pi R^3}{V_l + n_0 V_l \frac{4}{3}\pi R^3} = \frac{n_0 \frac{4}{3}\pi R^3}{1 + n_0 \frac{4}{3}\pi R^3} \tag{B.2}$$

From the definition of volume fraction, being $V_l + V_v + V_{nc} = V$ and dividing the LHS of the previous equation by $V$, it follows:

$$\frac{V_v}{V_l + V_v} = \frac{V_v/V}{(V_l + V_v)/V} = \frac{\alpha_v}{\alpha_v + \alpha_l} \tag{B.3}$$

so:

$$\frac{\alpha_v}{\alpha_v + \alpha_l} = \frac{n_0 \frac{4}{3}\pi R^3}{1 + n_0 \frac{4}{3}\pi R^3} \tag{B.4}$$

Rearranging Eq. (B.4), the vapor volume fraction reads:

$$\alpha_v = \alpha_l n_0 \frac{4}{3}\pi R^3 \tag{B.5}$$

From Eq. (B.5) the rate of fuel vaporization is calculated as:

$$\frac{D\alpha_v}{Dt} = \frac{D\left(\alpha_l n_0 \frac{4}{3}\pi R^3\right)}{Dt} = n_0 \frac{4}{3}\pi R^3 \frac{D\alpha_l}{Dt} + \alpha_l n_0 4\pi R^2 \frac{DR}{Dt} \tag{B.6}$$

From system (A.3) and Eq. (6):

$$\frac{D\alpha_l}{Dt} = -\alpha_l \nabla \cdot \mathbf{U} - \frac{\rho_v}{\rho + \alpha_{nc}(\rho_l - \rho_{nc})}\frac{D\alpha_v}{Dt} \tag{B.7}$$

The substitution of Eq. (B.7) in Eq. (B.6) leads to:

$$\frac{D\alpha_v}{Dt} = \frac{\alpha_l n_0 4\pi R^2 \frac{DR}{Dt}}{1 + n_0 \frac{4}{3}\pi R^3 \left(\frac{\rho + \alpha_{nc}(\rho_v - \rho_{nc})}{\rho + \alpha_{nc}(\rho_l - \rho_{nc})}\right)} \tag{B.8}$$

The formulation of the bubble growth rate $\frac{DR}{Dt}$, has been the main topic of several studies in the past [27,25,26]; in this work, the formulation from Rayleigh [27] is used:

$$\frac{DR}{Dt} = \text{sign}\big(p(R) - p_\infty\big)\sqrt{\frac{2}{3}\frac{p(R) - p_\infty}{\rho_l}} \tag{B.9}$$

where $p(R)$ is the pressure in the liquid at the bubble boundary and $p_\infty$ is the pressure at a large distance from the bubble. To model either the bubble growth and its collapse in a single equation, $p(R)$ is set in Eq. (B.9) to the vapor saturation pressure $p_{sat}$ and $p_\infty$ to the pressure inside the computational cell, so it follows:

$$\frac{DR}{Dt} = -(p - p_{sat})\sqrt{\frac{2}{3}\frac{1}{\rho_l|p - p_{sat}|}} = \begin{cases} -min(p - p_{sat}, 0)\sqrt{\frac{2}{3}\frac{1}{\rho_l|p-p_{sat}|}} & \text{if } p < p_{sat} \\ -max(p - p_{sat}, 0)\sqrt{\frac{2}{3}\frac{1}{\rho_l|p-p_{sat}|}} & \text{if } p > p_{sat} \end{cases} \tag{B.10}$$

which describes both the bubble grow and its collapse; as a consequence:

$$\frac{D\alpha_v}{Dt} = \begin{cases} \frac{3\alpha_v \frac{DR}{Dt}}{R + R^4 \frac{4}{3}\pi n_0 \left[\frac{\rho + \alpha_{nc}(\rho_v - \rho_{nc})}{\rho + \alpha_{nc}(\rho_l - \rho_{nc})}\right]} = -\frac{3\alpha_v max(p - p_{sat}, 0)\sqrt{\frac{2}{3}\frac{1}{\rho_l|p-p_{sat}|}}}{R + R^4 \frac{4}{3}\pi n_0 \left[\frac{\rho + \alpha_{nc}(\rho_v - \rho_{nc})}{\rho + \alpha_{nc}(\rho_l - \rho_{nc})}\right]} = \alpha_v \left(\frac{D\alpha_v}{Dt}\right)^+ & \text{if } p > p_{sat} \\ \frac{\alpha_l 4\pi n_0 R^2 \frac{DR}{Dt}}{1 + R^3 \frac{4}{3}\pi n_0 \left[\frac{\rho + \alpha_{nc}(\rho_v - \rho_{nc})}{\rho + \alpha_{nc}(\rho_l - \rho_{nc})}\right]} = -\frac{\alpha_l 4\pi n_0 R^2 min(p - p_{sat}, 0)\sqrt{\frac{2}{3}\frac{1}{\rho_l|p-p_{sat}|}}}{1 + R^3 \frac{4}{3}\pi n_0 \left[\frac{\rho + \alpha_{nc}(\rho_v - \rho_{nc})}{\rho + \alpha_{nc}(\rho_l - \rho_{nc})}\right]} = \alpha_l \left(\frac{D\alpha_v}{Dt}\right)^- & \text{if } p < p_{sat} \end{cases} \tag{B.11}$$

## Appendix C. Two-dimensional simulation of the evolution of the free-surface in a partially cavitating/condensating liquid column

The same numerical problem presented in Sec. 11 and described in Fig. 8 is simulated here in two dimensions. The aspect ratio of the two-dimensional domain was width/height = 0.5: the height of the domain is $\Delta y$ and the width along the transverse direction is $\Delta y/2$. Similarly to Sec. 11, simulations on two different grids have been performed, namely grid A (now 320×640 cells) and grid B (now 640 × 1280 cells); the two grids have the same cell aspect ratio equal to unity. The same benchmark quantities reported for the one-dimensional simulations has been selected to monitor the numerical properties of the solver: the position, sharpness and modeled velocity of the interface, the overall mass conservation and the instantaneous mass balance between the liquid fuel and the fuel vapor. The same boundary and initial conditions of the one-dimensional tests has been applied; for a fair comparison, also the results of this section are presented as in Sec. 11.

### *C.1. Cavitation test: results*

Starting from an hydrostatic distribution of the pressure in the domain, the liquid starts cavitating. Being the vapor lighter than the liquid, it moves upwards and pushes the non-condensable gas (air) out of the domain. Results of Fig. C.23 and Fig. C.24 show similar trends to those reported in Fig. 9; for the two-dimensional case, absolute values of the mass are larger if compared to the one-dimensional case, because now the domain is extended over the x-direction and the amount of mass in the domain is larger.

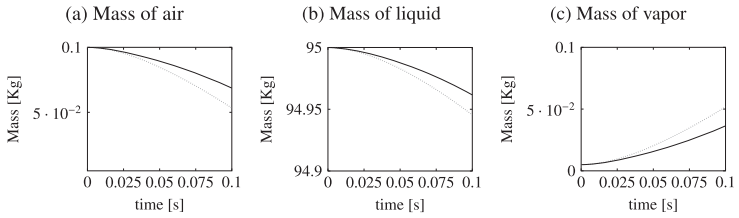


**Fig. C.23.** Two-dimensional cavitation problem, validation test case. Evolution in time of: (a) air mass; (b) liquid mass; (c) vapor mass for two different grids: .... grid A (320 × 640 cells); — grid B (640 × 1280 cells).

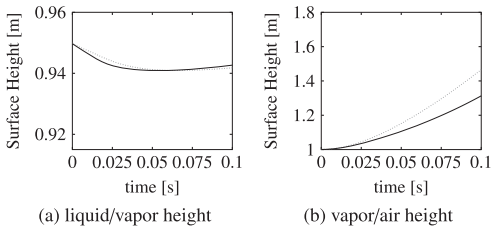


**Fig. C.24.** Two-dimensional cavitation problem. Evolution in time of the surface heights: (a) liquid/vapor; (b) air/vapor for two different grids: .... grid A (320 × 640 cells); — grid B (640 × 1280 cells).

The evolution of the two surface fronts is shown in Fig. C.25. The black solid line is the contour line of $\alpha_v = 0.5$, that bounds the region of the vapor: the upper line in Fig. C.25 is then the vapor-air interface, while the lower line is the vapor-liquid interface.

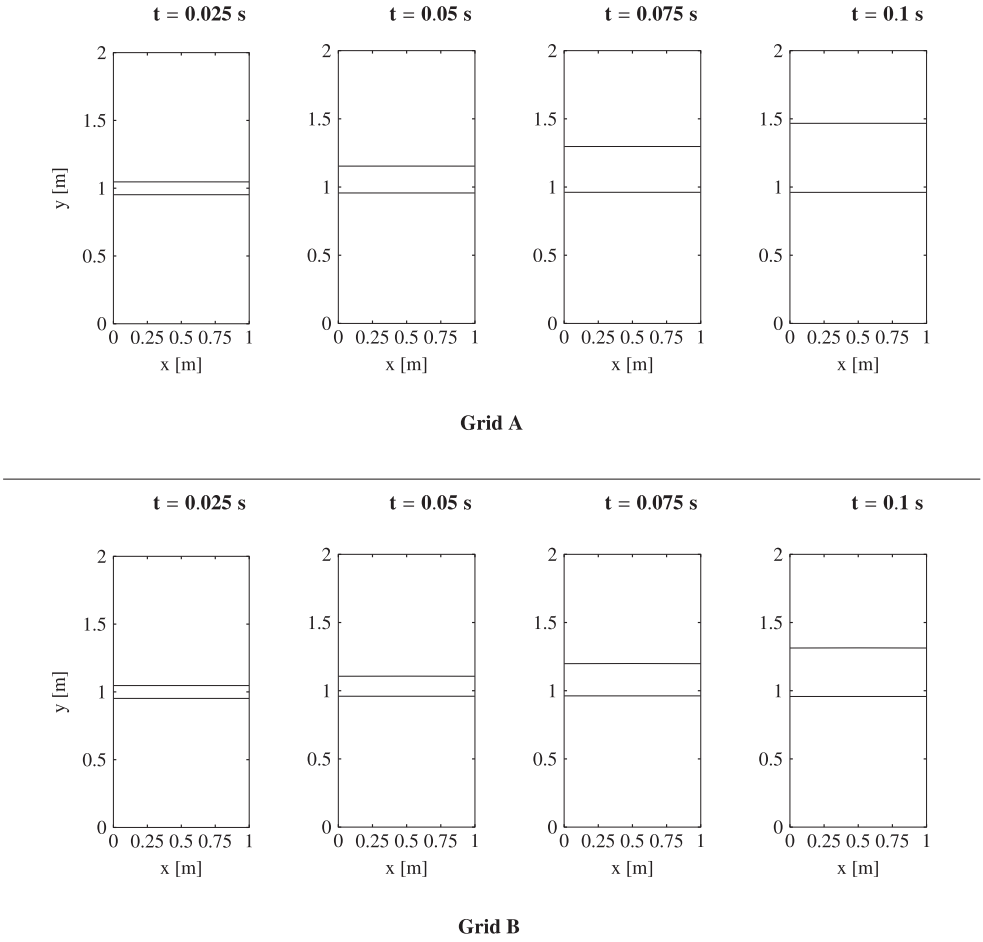


**Fig. C.25.** Two-dimensional cavitation problem. Evolution in time of the void fraction profiles of the fuel-vapor, that bound the vapor region, from 0.025 to 0.1 s. Top) grid A, 320 × 640 cells; bottom) grid B, 640 × 1280 cells. Legend: $\alpha_v$ —.

The liquid/vapor and the air/vapor interface velocities, calculated by Eq. (53), are reported in Fig. C.26 for the two-dimensional simulations. Again, they are very similar to the values achieved in Fig. 12; this is not surprising, because the free-surface in this specific test-case evolves mostly over a main direction.

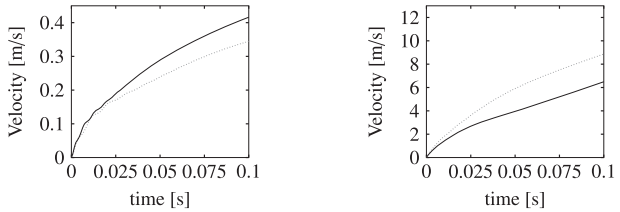


(a) modeled liquid/vapor surface velocity (b) modeled vapor/air surface velocity

**Fig. C.26.** Two-dimensional cavitation problem, validation test case. Evolution in time of the mean interface velocity: (a) liquid/vapor; (b) air/vapor on two different grids: .... grid A (320 × 640 cells); — grid B (640 × 1280 cells).

Finally, the mass of each phase fraction has been monitored to compute the time step continuity error and the mass conservation error in the domain (Fig. C.27 and Table C.10). They are still very limited, in accordance to what it has been shown for the one-dimensional test case. This proves that the numerical accuracy of the solver is maintained also in presence of cavitation and multi-dimensional domains.

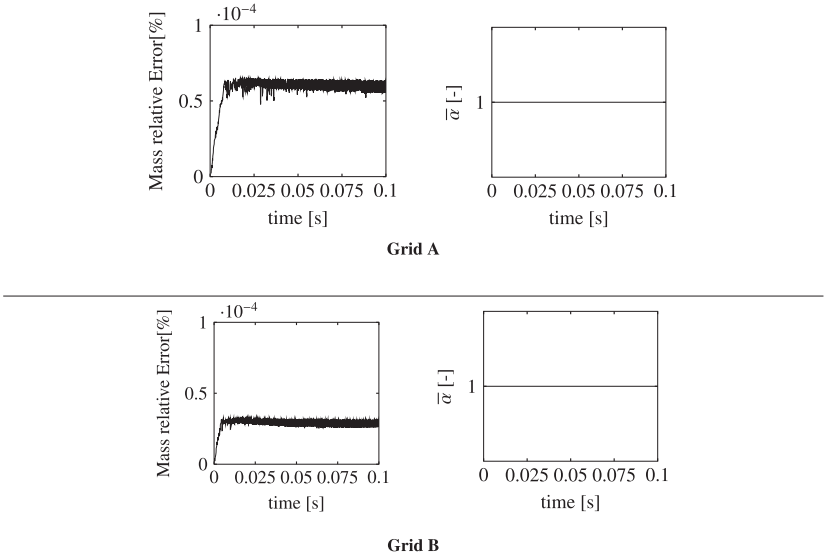


**Fig. C.27.** Two-dimensional cavitation test case, evolution in time of: left) mass relative error; right) sum of the volume-weighted void fractions (see Eq. (57)). Grid A: 320 × 640 cells. Grid B: 640 × 1280 cells.

**Table C.10**
Relative error in the global mass conservation for the cavitation test case.

| No. cells | 320 × 640 | 640 × 1280 |
|---|---|---|
| $E_{global}$% | 0.106 | 0.026 |

## C.2. Condensation test: results

Similarly to what has been done in Sec. 11, the distribution of the phase-fractions derived from the calculation of the two-dimensional liquid column problem with cavitation is set as initial condition. Vapor condensation is artificially triggered by changing the threshold value of the liquid saturation pressure; as a result, the vapor changes direction of its motion and a suction of non-condensable gas (air) from the upper boundary is observed. Fig. C.28b shows the evolution of the global mass of the separate phases in the domain in time.

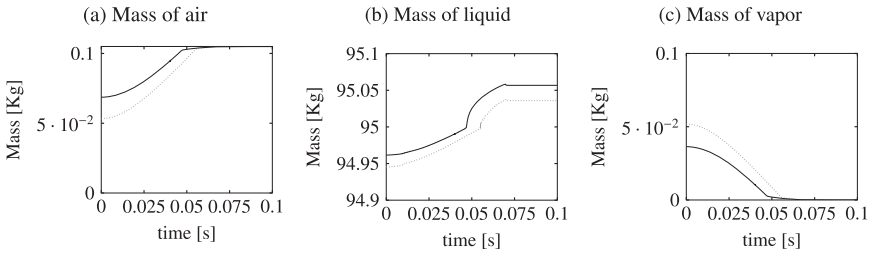


**Fig. C.28.** Two-dimensional condensation problem, validation test case. Evolution in time of: (a) air mass; (b) liquid mass; (c) vapor mass for two different grids: .... grid A (320 × 640 cells); — grid B (640 × 1280 cells).

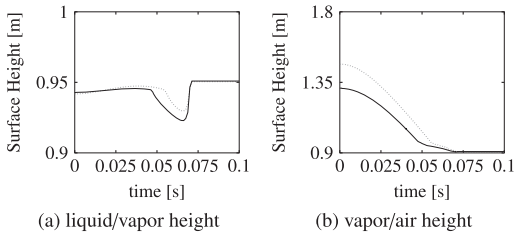


**Fig. C.29.** Two-dimensional condensation problem, validation test case. Evolution in time of the surface heights: (a) liquid/vapor; (b) air/vapor for two different grids: .... grid A (320 × 640 cells); — grid B (640 × 1280 cells).

The evolution of the two surfaces fronts (liquid/vapor and air/vapor) is shown in Fig. C.30 for a duration of 0.5 s. The black solid line is the iso-contour line of the phase fraction of the vapor at 0.5. The upper-line locates the vapor-air interface, while the lower line is the vapor-liquid interface; the region of the fuel-vapor is therefore bounded by these two lines. Approximately at $t = 0.6$ s, the fuel-vapor is fully condensed (Fig. C.29) and the visualization of two interfaces is not possible anymore; for clarity, a black dotted line for the liquid-air interface is used at 0.75 s and 0.1 s.

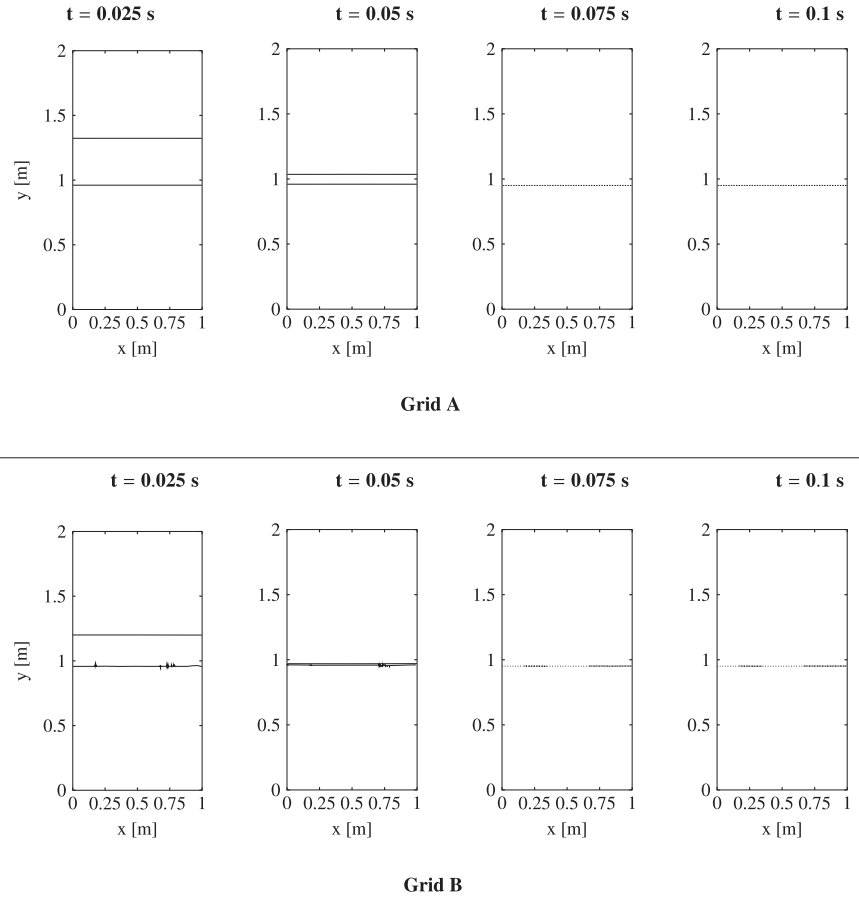


**Fig. C.30.** Two-dimensional condensation problem. Evolution in time of the iso-contour line of the fuel-vapor $\alpha_v = 0.5$, that bounds the vapor region, from 0.025 to 0.1 s. Top) grid A, 320 × 640 cells; bottom) grid B, 640 × 1280 cells. Legend: $\alpha_v$ —.

The liquid/vapor and the air/vapor interface velocities, calculated by Eq. (53), are plotted in Fig. C.31. Again, they are very similar to the values achieved in Fig. 17 for the one-dimensional case; this is not surprising, because the free-surface in this specific test-case evolves mostly in one-direction and also the one-dimensional domain is sufficient to describe the evolution of the experiment.

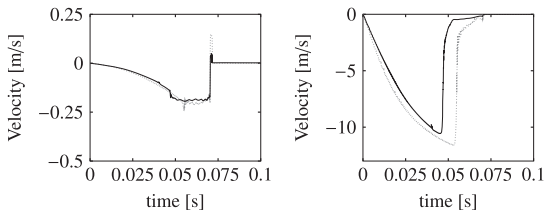


(a) liquid/vapor surface velocity (b) vapor/air surface velocity

**Fig. C.31.** Two-dimensional condensation problem, validation test case. Evolution in time of the mean interface velocity: (a) liquid/vapor surface velocity and (b) air/vapor surface velocity. `interPhaseChangeMixingFoam` behavior using two different discretizations: ..... 320 × 640 cells; — 640 × 1280 cells.

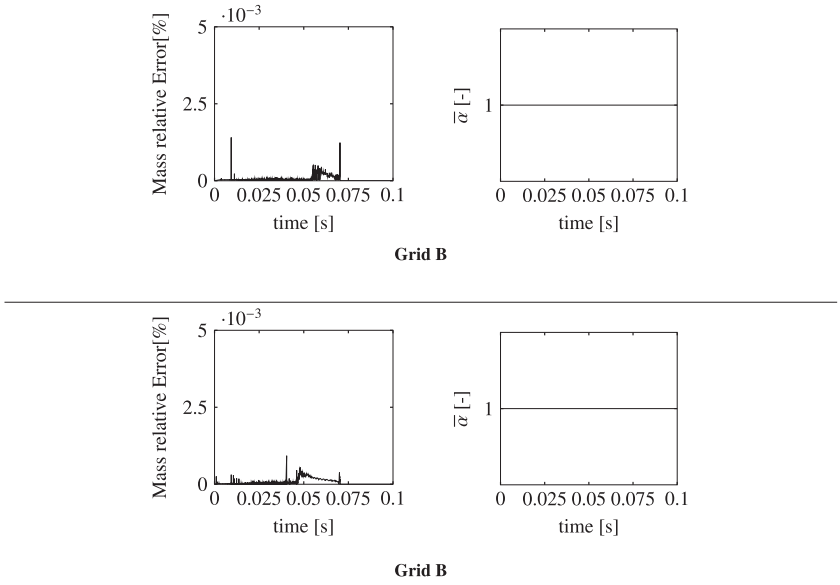


**Fig. C.32.** Two-dimensional condensation test case, evolution in time of: left) mass relative error; right) sum of the volume-weighted void fractions (see Eq. (57)). Grid A: 320 × 640 cells. Grid B: 640 × 1280 cells.

**Table C.11**
Relative (percentage) error on global mass conservation for condensation test case.

| No. cells | 320 × 640 | 640 × 1280 |
|---|---|---|
| $E_{global}$% | 0.1496 | 0.1385 |

Finally, Fig. C.32 shows that also for the two-dimensional simulations, the global errors for the two grid resolutions tested are still very limited (Table C.11) and that the solver is very accurate in the handling of the phase change with multi-dimensional domains. It is important to remark that the error peak presents at 0.075 s is smaller than the one observed in the one-dimensional case (Fig. 18): in multi-dimensional problems, the influence of the boundary conditions on the solution is smaller, so the errors in the solution of the linear systems can be spread over the multiple directions. This is not possible in a one-dimensional test case.

## References

[1] B. Yin, S. Yu, H. Jia, J. Yu, Numerical research of diesel spray and atomization coupled cavitation by large eddy simulation (LES) under high injection pressure, Int. J. Heat Fluid Flow 59 (2016) 1–9, https://doi.org/10.1016/j.ijheatfluidflow.2016.01.005, http://www.sciencedirect.com/science/article/pii/S0142727X16300029.
[2] S. Makhlouf, J. Hélie, G. Grimoux, J. Cousin, L. Gestri, A. Wood, G. Wigley, Large eddy simulation of cavitation and atomization in injector flows using OpenFOAM, in: ICLASS 2012, 12th Triennial Int. Conference on Liquid Atomization and Spray Systems, Heidelberg, Germany, 2012.
[3] O.J. Soriano-Palao, M. Sommerfeld, A. Burkhardt, Modelling the influence of the nozzle geometry on the primary breakup of diesel jets, Int. J. Spray Combust. Dyn. 6 (2) (2014) 113–146, https://doi.org/10.1260/1756-8277.6.2.113.
[4] J.M. Shi, K. Wenzlawski, J. Helie, H. Nuglish, J. Cousin, URANS and SAS analysis of flow dynamics in a GDI nozzle, in: ILASS – Europe 2010, 23rd Annual Conference on Liquid Atomization and Spray Systems, Brno, Czech Republic, September 2010, 2010.
[5] M. Gavaises, A. Andriotis, D. Papoulias, N. Mitroglou, A. Theodorakakos, Characterization of string cavitation in large-scale diesel nozzles with tapered holes, Phys. Fluids 21 (5) (2009) 052107, https://doi.org/10.1063/1.3140940.
[6] H. Chaves, M. Knapp, A. Kubitzek, F. Obermeier, et al., Experimental Study of Cavitation in the Nozzle Hole of Diesel Injectors Using Transparent Nozzles, SAE Technical Paper 950290, 1995.
[7] U. Iben, A. Morozov, E. Winklhofer, F. Wolf, Laser-pulse interferometry applied to high-pressure fluid flow in micro channels, Exp. Fluids 50 (3) (2011) 597–611.
[8] J. Serras-Pereira, Z. van Romunde, P. Aleiferis, D. Richardson, S. Wallace, R. Cracknell, Cavitation, primary break-up and flash boiling of gasoline, iso-octane and n-pentane with a real-size optical direct-injection nozzle, Fuel 89 (9) (2010) 2592–2607, https://doi.org/10.1016/j.fuel.2010.03.0301, http://www.sciencedirect.com/science/article/pii/S0016236110001225.
[9] Z. Chen, Z. He, W. Shang, L. Duan, H. Zhou, G. Guo, W. Guan, Experimental study on the effect of nozzle geometry on string cavitation in real-size optical diesel nozzles and spray characteristics, Fuel 232 (2018) 562–571, https://doi.org/10.1016/j.fuel.2018.05.132, http://www.sciencedirect.com/science/article/pii/S0016236118309670.
[10] E. Roohi, A.P. Zahiri, M. Passandideh-Fard, Numerical simulation of cavitation around a two-dimensional hydrofoil using VoF method and LES turbulence model, Appl. Math. Model. 37 (9) (2013) 6469–6488, https://doi.org/10.1016/j.apm.2012.09.002.
[11] E. Kawakami, R. Arndt, Investigation of the behavior of ventilated supercavities, ASME J. Fluids Eng. 133 (9) (2011), https://doi.org/10.1115/1.4004911.
[12] J.H. Kim, K. Nishida, H. Hiroyasu, Characteristics of the internal flow in a diesel injection nozzle, Int. J. Fluid Mech. Res. 24 (1–3) (1997) 34–44.

[13] R. Husson, L. Ganippa, H. Zhao, Flow and cavitation structure in a scaled-up multi hole optical diesel nozzle, in: 22nd European Conference on Liquid Atomization and Spray Systems, ILASS, 8-10 September 2008, Como, Italy, 2008.
[14] A. Andriotis, M. Gavaises, Influence of vortex flow and cavitation on near-nozzle diesel spray dispersion angle, At. Sprays 19 (3) (2009) 247–261.
[15] A.J. Reynolds, Thermo-fluid dynamic theory of two-phase flow. By M. ISHIL Eyrolles 1975. 248 pp. 83f or $ 2160, J. Fluid Mech. 78 (03) (1976) 638, https://doi.org/10.1017/s0022112076212656.
[16] T.J. Hanratty, T. Theofanous, J.M. Delhaye, J. Eaton, J. McLaughlin, A. Prosperetti, S. Sundaresan, G. Tryggvason, Workshop findings, Int. J. Multiph. Flow 29 (7) (2003) 1047–1059, http://www.princeton.edu/cbe/people/faculty/sundaresan/group/publications/pdf/99.pdf.
[17] G. Tryggvason, B. Bunner, A. Esmaeeli, D. Juric, N. Al-Rawahi, B. Tauber, J. Han, S. Nas, Y. Jan, A front-tracking method for the computations of multiphase flow, J. Comput. Phys. 169 (2001) 708–759.
[18] J. Du, B. Fix, J. Glimm, X. Jia, X. Li, Y. Li, L. Wu, A simple package for front tracking, J. Comput. Phys. 213 (2006) 613–628.
[19] C. Hirt, B. Nichols, Volume of fluid (VOF) method for the dynamics of free boundaries, J. Comput. Phys. 39 (1) (1981) 201–225, https://doi.org/10.1016/0021-9991(81)90145-5.
[20] J.A. Sethian, P. Smereka, Level set methods for fluid interfaces, Annu. Rev. Fluid Mech. 35 (1) (2003) 341–372, https://doi.org/10.1146/annurev.fluid.35.101101.161105.
[21] M. Sussman, E.G. Puckett, A coupled level set and volume-of-fluid method for computing 3d and axisymmetric incompressible two-phase flows, J. Comput. Phys. 162 (2) (2000) 301–337, https://doi.org/10.1006/jcph.2000.6537, http://www.sciencedirect.com/science/article/pii/S0021999100965379.
[22] T. Ménard, S. Tanguy, A. Berlemont, Coupling level set/VoF/ghost fluid methods: validation and application to 3d simulation of the primary break-up of a liquid jet, Int. J. Multiph. Flow 33 (5) (2007) 510–524, https://doi.org/10.1016/j.ijmultiphaseflow.2006.11.001, http://www.sciencedirect.com/science/article/pii/S0301932206001832.
[23] Z. Wang, J. Yang, B. Koo, F. Stern, A coupled level set and volume-of-fluid method for sharp interface simulation of plunging breaking waves, Int. J. Multiph. Flow 35 (3) (2009) 227–246, https://doi.org/10.1016/j.ijmultiphaseflow.2008.11.004, http://www.sciencedirect.com/science/article/pii/S0301932208001833.
[24] M.S. Plesset, Cavitating Flows, Tech. rep., Division of Engineering and Applied Science, California Institute of Technology, 1969.
[25] M.S. Plesset, The dynamics of cavitation bubbles, J. Appl. Mech. 16 (1949) 277–282, http://resolver.caltech.edu/CaltechAUTHORS:20140808-114249321.
[26] M.S. Plesset, A. Prosperetti, Bubble dynamics and cavitation, Annu. Rev. Fluid Mech. 9 (1) (1977) 145–185, https://doi.org/10.1146/annurev.fl.09.010177.001045.
[27] O.F. Lord Rayleigh, VIII. On the pressure developed in a liquid during the collapse of a spherical cavity, Lond. Edinb. Dublin Philos. Mag. J. Sci. 34 (200) (1917) 94–98, https://doi.org/10.1080/14786440808635681.
[28] M.-G. Mithun, P. Koukouvinis, M. Gavaises, Numerical simulation of cavitation and atomization using a fully compressible three-phase model, Phys. Rev. Fluids 3 (2018) 064304, https://doi.org/10.1103/PhysRevFluids.3.064304.
[29] Y. Wang, R.D. Reitz, Eulerian two-phase flow CFD simulation using a compressible and equilibrium eight-equation model, in: ILASS 2015, 27th Annual Conference on Liquid Atomization and Spray Systems, Raleigh, NC, 2015.
[30] R. Saurel, F. Petitpas, R. Abgrall, Modelling phase transition in metastable liquids: application to cavitating and flashing flows, J. Fluid Mech. 607 (2008) 313–350, https://doi.org/10.1017/S0022112008002061.
[31] F. Orley, T. Trummler, S. Hickel, M.S. Mihatsch, S.J. Schmidt, N.A. Adams, Large-eddy simulation of cavitating nozzle flow and primary jet break-up, Phys. Fluids 27 (8) (2015) 086101, https://doi.org/10.1063/1.4928701.
[32] W. Edelbauer, Numerical simulation of cavitating injector flow and liquid spray break-up by combination of Eulerian–Eulerian and volume-of-fluid methods, Comput. Fluids 144 (2017) 19–33, https://doi.org/10.1016/j.compfluid.2016.11.019, http://www.sciencedirect.com/science/article/pii/S0045793016303747.
[33] M.-G. Mithun, P. Koukouvinis, M. Gavaises, Numerical simulation of cavitation and atomization using a fully compressible three-phase model, Phys. Rev. Fluids 3 (2018) 064304, https://doi.org/10.1103/PhysRevFluids.3.064304.
[34] S. Quan, J. Lou, D. Schmidt, Modeling merging and breakup in the moving mesh interface tracking method for multiphase flow simulations, J. Comput. Phys. 228 (2009).
[35] M. Altimira, L. Fuchs, Numerical investigation of throttle flow under cavitating conditions, Int. J. Multiph. Flow 75 (2015) 124–136, https://doi.org/10.1016/j.ijmultiphaseflow.2015.05.006, http://www.sciencedirect.com/science/article/pii/S0301932215001238.
[36] Z.X. He, Z. Shao, Z.W. Zhou, X.C. Tao, Experimental study of hydraulic flip phenomenon inside diesel nozzles using diesel and biodiesel, in: Advances in Manufacturing Science and Engineering V, in: Advanced Materials Research, Trans Tech Publications, vol. 945, 2014, pp. 940–943.
[37] C. Soteriou, R. Andrews, M. Smith, Direct Injection Diesel Sprays and the Effect of Cavitation and Hydraulic Flip on Atomization, SAE Technical Paper, SAE Int., 1995.
[38] C. Soteriou, R. Andrews, M. Smith, Further studies of cavitation and atomization in diesel injection, in: International Fuels & Lubricants Meeting & Exposition, SAE International, 1999.
[39] A. Sou, S. Hosokawa, A. Tomiyama, Effects of cavitation in a nozzle on liquid jet atomization, Int. J. Heat Mass Transf. 50 (17) (2007) 3575–3582, https://doi.org/10.1016/j.ijheatmasstransfer.2006.12.033, http://www.sciencedirect.com/science/article/pii/S0017931007001019.
[40] H. Yu, L. Goldsworthy, P. Brandner, V. Garaniya, Development of a compressible multiphase cavitation approach for diesel spray modelling, Appl. Math. Model. 45 (2017) 705–727, https://doi.org/10.1016/j.apm.2017.01.035, http://www.sciencedirect.com/science/article/pii/S0307904X17300410.
[41] M. Cailloux, J. Helie, J. Reveillon, F.X. Demoulin, Large eddy simulation of a cavitating multiphase flow for liquid injection, J. Phys. Conf. Ser. 656 (2015) 012081, https://doi.org/10.1088/1742-6596/656/1/012081.
[42] R.F. Kunz, D.A. Boger, D.R. Stinebring, T.S. Chyczewski, J.W. Lindau, H.J. Gibeling, S. Venkateswaran, T. Govindan, A preconditioned Navier–Stokes method for two-phase flows with application to cavitation prediction, Comput. Fluids 29 (8) (2000) 849–875, https://doi.org/10.1016/S0045-7930(99)00039-0.
[43] J. Sauer, G.H. Schnerr, Unsteady Cavitating Flow – A New Cavitation Model Based on A Modified Front Capturing Method And Bubble Dynamics, 2000.
[44] W. Yuan, G.H. Schnerr, Numerical simulation of two-phase flow in injection nozzles: interaction of cavitation and external jet formation, J. Fluids Eng. 125 (6) (2004) 963–969, https://doi.org/10.1115/1.1625687.
[45] H. Liu, W. Zhang, M. Jia, Y. Yan, Y. He, An improved method for coupling the in-nozzle cavitation with multi-fluid-quasi-VoF model for diesel spray, Comput. Fluids 177 (2018) 20–32, https://doi.org/10.1016/j.compfluid.2018.09.017, http://www.sciencedirect.com/science/article/pii/S0045793018306947.
[46] P. Koukouvinis, H. Naseri, M. Gavaises, Performance of turbulence and cavitation models in prediction of incipient and developed cavitation, Int. J. Eng. Res. 18 (4) (2017) 333–350, https://doi.org/10.1177/1468087416658604.
[47] B. Duret, R. Canu, J. Reveillon, F. Demoulin, A pressure based method for vaporizing compressible two-phase flows with interface capturing approach, Int. J. Multiph. Flow 108 (2018) 42–50, https://doi.org/10.1016/j.ijmultiphaseflow.2018.06.022, http://www.sciencedirect.com/science/article/pii/S0301932218302799.
[48] C.P. Egerer, S.J. Schmidt, S. Hickel, N.A. Adams, Efficient implicit LES method for the simulation of turbulent cavitating flows, J. Comput. Phys. 316 (2016) 453–469, https://doi.org/10.1016/j.jcp.2016.04.021, http://www.sciencedirect.com/science/article/pii/S0021999116300626.
[49] E. Lauer, X. Hu, S. Hickel, N. Adams, Numerical modelling and investigation of symmetric and asymmetric cavitation bubble dynamics, Comput. Fluids 69 (2012) 1–19, https://doi.org/10.1016/j.compfluid.2012.07.020, http://www.sciencedirect.com/science/article/pii/S0045793012002885.

[50] S. Hysing, S. Turek, D. Kuzmin, N. Parolini, E. Burman, S. Ganesan, L. Tobiska, Quantitative benchmark computations of two-dimensional bubble dynamics, Int. J. Numer. Methods Fluids 60 (11) (2009) 1259–1288.

[51] J. Klostermann, K. Schaake, R. Schwarze, Numerical simulation of a single rising bubble by VoF with surface compression, Int. J. Numer. Methods Fluids 71 (8) (2013) 960–982, https://doi.org/10.1002/fld.3692.

[52] A. Sou, B. Biçer, A. Tomiyama, Numerical simulation of incipient cavitation flow in a nozzle of fuel injector, Comput. Fluids 103 (2014) 42–48, https://doi.org/10.1016/j.compfluid.2014.07.011.

[53] The OpenFOAM Foundation, OpenFOAM user guide, https://cfd.direct/openfoam/user-guide.

[54] R. Issa, Solution of the implicitly discretised fluid flow equations by operator-splitting, J. Comput. Phys. 62 (1) (1986) 40–65, https://doi.org/10.1016/0021-9991(86)90099-9, http://www.sciencedirect.com/science/article/pii/0021999186900999.

[55] H. Weller, A New Approach to VOF-Based Interface Capturing Methods for Incompressible and Compressible Flow, Technical report TR/HGW/04, OpenCFD Ltd., 2008.

[56] W. Yuan, J. Sauer, G.H. Schnerr, Modeling and computation of unsteady cavitation flows in injection nozzles, Méc. Ind. 2 (5) (2001) 383–394, https://doi.org/10.1016/s1296-2139(01)01120-4.

[57] Eddy Large Simulation for Incompressible Flows, Springer-Verlag, 2006.

[58] S. Pope, Turbulent Flows, Cambridge University Press, 2000.

[59] M. Lesieur, O. Metais, P. Comte, Large-Eddy Simulations of Turbulence, Cambridge University Press, 2005.

[60] X. Hu, N. Adams, Scale separation for implicit large eddy simulation, J. Comput. Phys. 230 (19) (2011) 7240–7249, https://doi.org/10.1016/j.jcp.2011.05.023, http://www.sciencedirect.com/science/article/pii/S0021999111003342.

[61] B. Knaepen, O. Debliquy, D. Carati, Large-eddy simulation without filter, J. Comput. Phys. 205 (1) (2005) 98–107, https://doi.org/10.1016/j.jcp.2004.10.037, http://www.sciencedirect.com/science/article/pii/S0021999104004590.

[62] M. Gavaises, F. Villa, P. Koukouvinis, M. Marengo, J.-P. Franc, Visualisation and LES simulation of cavitation cloud formation and collapse in an axisymmetric geometry, Int. J. Multiph. Flow 68 (2015) 14–26, https://doi.org/10.1016/j.ijmultiphaseflow.2014.09.008, http://www.sciencedirect.com/science/article/pii/S0301932214001700.

[63] R.E. Bensow, G. Bark, Implicit LES predictions of the cavitating flow on a propeller, J. Fluids Eng. 132 (4) (2010) 041302, https://doi.org/10.1115/1.4001342.

[64] X. Luo, B. Ji, X. Peng, H. Xu, M. Nishi, Numerical simulation of cavity shedding from a three-dimensional twisted hydrofoil and induced pressure fluctuation by large-eddy simulation, J. Fluids Eng. 134 (4) (2012) 041202, https://doi.org/10.1115/1.4006416.

[65] Y. Chen, X. Chen, J. Li, Z. Gong, C. Lu, Large eddy simulation and investigation on the flow structure of the cascading cavitation shedding regime around 3d twisted hydrofoil, Ocean Eng. 129 (2017) 1–19, https://doi.org/10.1016/j.oceaneng.2016.11.012, http://www.sciencedirect.com/science/article/pii/S0029801816305121.

[66] B. Huang, Y. Zhao, G. Wang, Large eddy simulation of turbulent vortex-cavitation interactions in transient sheet/cloud cavitating flows, Comput. Fluids 92 (2014) 113–124, https://doi.org/10.1016/j.compfluid.2013.12.024, http://www.sciencedirect.com/science/article/pii/S0045793013005161.

[67] B. Ji, X. Luo, R.E. Arndt, X. Peng, Y. Wu, Large eddy simulation and theoretical investigations of the transient cavitating vortical flow structure around a NACA66 hydrofoil, Int. J. Multiph. Flow 68 (2015) 121–134, https://doi.org/10.1016/j.ijmultiphaseflow.2014.10.008, http://www.sciencedirect.com/science/article/pii/S0301932214001967.

[68] J. Reboud, B. Stutz, O. Coutier, Two-phase flow structure of cavitation: experiments and modelling of unsteady effects, in: 3rd International Symposium on Cavitation, April 1998, Grenoble, France, 1998.

[69] O. Coutier-Delgosha, R. Fortes-Patella, J.L. Reboud, Evaluation of the turbulence model influence on the numerical simulations of unsteady cavitation, J. Fluids Eng. 125 (1) (2003) 38, https://doi.org/10.1115/1.1524584.

[70] B. Huang, A. Ducoin, Y.L. Young, Physical and numerical investigation of cavitating flows around a pitching hydrofoil, Phys. Fluids 25 (10) (2013) 102109, https://doi.org/10.1063/1.4825156.

[71] B. Huang, Y.L. Young, G. Wang, W. Shyy, Combined experimental and computational investigation of unsteady structure of sheet/cloud cavitation, J. Fluids Eng. 135 (7) (2013) 071301, https://doi.org/10.1115/1.4023650.

[72] Y. Long, X. ping Long, B. Ji, W. xin Huai, Z. dong Qian, Verification and validation of URANS simulations of the turbulent cavitating flow around the hydrofoil, J. Hydrodyn. Ser. B 29 (4) (2017) 610–620, https://doi.org/10.1016/S1001-6058(16)60774-6, http://www.sciencedirect.com/science/article/pii/S1001605816607746.

[73] C. Hirt, B. Nichols, Volume of fluid (VoF) method for the dynamics of free boundaries, J. Comput. Phys. 39 (1) (1981) 201–225, https://doi.org/10.1016/0021-9991(81)90145-5.

[74] W.T.-F. Section, H.G. Weller, The Development of a New Flame Area Combustion Model Using Conditional Averaging, 1993.

[75] K.E. Wardle, H.G. Weller, Hybrid multiphase CFD solver for coupled dispersed/segregated flows in liquid-liquid extraction, Int. J. Chem. Eng. 2013 (2013) 1–13, https://doi.org/10.1155/2013/128936, article ID 128936.

[76] A. Baraldi, M. Dodd, A. Ferrante, A mass-conserving volume-of-fluid method: volume tracking and droplet surface-tension in incompressible isotropic turbulence, Comput. Fluids 96 (2014) 322–337, https://doi.org/10.1016/j.compfluid.2013.12.018, http://www.sciencedirect.com/science/article/pii/S0045793013005100.

[77] D. Bothe, S. Fleckenstein, A volume-of-fluid-based method for mass transfer processes at fluid particles, Chem. Eng. Sci. 101 (2013) 283–302, https://doi.org/10.1016/j.ces.2013.05.029, http://www.sciencedirect.com/science/article/pii/S0009250913003606.

[78] S. Fleckenstein, D. Bothe, A volume-of-fluid-based numerical method for multi-component mass transfer with local volume changes, J. Comput. Phys. 301 (2015) 35–58, https://doi.org/10.1016/j.jcp.2015.08.011, http://www.sciencedirect.com/science/article/pii/S0021999115005306.

[79] A. Weiner, D. Bothe, Advanced subgrid-scale modeling for convection-dominated species transport at fluid interfaces with application to mass transfer from rising bubbles, J. Comput. Phys. 347 (2017) 261–289, https://doi.org/10.1016/j.jcp.2017.06.040, http://www.sciencedirect.com/science/article/pii/S0021999117304941.

[80] D. Spalding, A Method for Computing Steady and Unsteady Flows Possessing Discontinuities of Density, Cham report 910/2, 1974.

[81] G.H. Schnerr, J. Sauer, Physical and numerical modeling of unsteady cavitation dynamics, in: ICMF-2001, 4th International Conference on Multiphase Flow, 2001.

[82] J. Brackbill, D. Kothe, C. Zemach, A continuum method for modeling surface tension, J. Comput. Phys. 100 (2) (1992) 335–354, https://doi.org/10.1016/0021-9991(92)90240-Y, http://www.sciencedirect.com/science/article/pii/002199919290240Y.

[83] S. Popinet, An accurate adaptive solver for surface-tension-driven interfacial flows, J. Comput. Phys. 228 (16) (2009) 5838–5866, https://doi.org/10.1016/j.jcp.2009.04.042, http://www.sciencedirect.com/science/article/pii/S002199910900240X.

[84] D. Gueyffier, J. Li, A. Nadim, R. Scardovelli, S. Zaleski, Volume-of-fluid interface tracking with smoothed surface stress methods for three-dimensional flows, J. Comput. Phys. 152 (2) (1999) 423–456, https://doi.org/10.1006/jcph.1998.6168, http://www.sciencedirect.com/science/article/pii/S002199919896168X.

[85] R.P. Fedkiw, T. Aslam, B. Merriman, S. Osher, A non-oscillatory Eulerian approach to interfaces in multimaterial flows (the ghost fluid method), J. Comput. Phys. 152 (2) (1999) 457–492, https://doi.org/10.1006/jcph.1999.6236, http://www.sciencedirect.com/science/article/pii/S0021999199962368.

[86] S. Popinet, S. Zaleski, Int. J. Numer. Methods Fluids 30 (6) (1999) 775–793, https://doi.org/10.1002/(SICI)1097-0363(19990730)30:6<775::AID-FLD864>3.0.CO;2-#, https://onlinelibrary.wiley.com/doi/abs/10.1002/%28SICI%291097-0363%2819990730%2930%3A6%3C775%3A%3AAID-FLD864%3E3.0.CO%3B2-%23.

[87] M.O. Abu-Al-Saud, S. Popinet, H.A. Tchelepi, A conservative and well-balanced surface tension model, J. Comput. Phys. 371 (2018) 896–913, https://doi.org/10.1016/j.jcp.2018.02.022, http://www.sciencedirect.com/science/article/pii/S0021999118301049.

[88] M. Sussman, K. Smith, M. Hussaini, M. Ohta, R. Zhi-Wei, A sharp interface method for incompressible two-phase flows, J. Comput. Phys. 221 (2) (2007) 469–505, https://doi.org/10.1016/j.jcp.2006.06.020, http://www.sciencedirect.com/science/article/pii/S0021999106002981.

[89] O. Desjardins, V. Moureau, H. Pitsch, An accurate conservative level set/ghost fluid method for simulating turbulent atomization, J. Comput. Phys. 227 (18) (2008) 8395–8416, https://doi.org/10.1016/j.jcp.2008.05.027, http://www.sciencedirect.com/science/article/pii/S0021999108003112.

[90] E. Olsson, G. Kreiss, A conservative level set method for two phase flow, J. Comput. Phys. 210 (1) (2005) 225–246, https://doi.org/10.1016/j.jcp.2005.04.007, http://www.sciencedirect.com/science/article/pii/S0021999105002184.

[91] R.W. Houim, K.K. Kuo, A ghost fluid method for compressible reacting flows with phase change, J. Comput. Phys. 235 (2013) 865–900, https://doi.org/10.1016/j.jcp.2012.09.022, http://www.sciencedirect.com/science/article/pii/S0021999112005530.

[92] S. Vincent, J. Larocque, D. Lacanette, A. Toutant, P. Lubin, P. Sagaut, Numerical simulation of phase separation and a priori two-phase LES filtering, in: Special Issue of the "Turbulence and Interaction-TI2006" Conference, Comput. Fluids 37 (7) (2008) 898–906, https://doi.org/10.1016/j.compfluid.2007.02.017, http://www.sciencedirect.com/science/article/pii/S0045793007001569.

[93] A. Toutant, E. Labourasse, O. Lebaigue, O. Simonin, DNS of the interaction between a deformable buoyant bubble and a spatially decaying turbulence: a priori tests for LES two-phase flow modelling, in: Special Issue of the "Turbulence and Interaction-TI2006" Conference, Comput. Fluids 37 (7) (2008) 877–886, https://doi.org/10.1016/j.compfluid.2007.03.019, http://www.sciencedirect.com/science/article/pii/S004579300700165X.

[94] E. Labourasse, D. Lacanette, A. Toutant, P. Lubin, S. Vincent, O. Lebaigue, J.-P. Caltagirone, P. Sagaut, Towards large eddy simulation of isothermal two-phase flows: governing equations and a priori tests, Int. J. Multiph. Flow 33 (1) (2007) 1–39, https://doi.org/10.1016/j.ijmultiphaseflow.2006.05.010.

[95] M. Herrmann, A sub-grid surface dynamics model for sub-filter surface tension induced interface dynamics, Comput. Fluids 87 (2013) 92–101, https://doi.org/10.1016/j.compfluid.2013.02.008, uSNCCM Moving Boundaries, http://www.sciencedirect.com/science/article/pii/S0045793013000637.

[96] P. Liovic, D. Lakehal, Subgrid-scale modelling of surface tension within interface tracking-based large eddy and interface simulation of 3d interfacial flows, Comput. Fluids 63 (2012) 27–46, https://doi.org/10.1016/j.compfluid.2012.03.019, http://www.sciencedirect.com/science/article/pii/S0045793012001168.

[97] W. Aniszewski, A. Bogusławski, M. Marek, A. Tyliszczak, A new approach to sub-grid surface tension for LES of two-phase flows, J. Comput. Phys. 231 (21) (2012) 7368–7397, https://doi.org/10.1016/j.jcp.2012.07.016, http://www.sciencedirect.com/science/article/pii/S0021999112003890.

[98] W. Aniszewski, Improvements, testing and development of the ADM-$\tau$ sub-grid surface tension model for two-phase LES, J. Comput. Phys. 327 (2016) 389–415, https://doi.org/10.1016/j.jcp.2016.09.033, http://www.sciencedirect.com/science/article/pii/S0021999116304545.

[99] A. Toutant, E. Labourasse, O. Lebaigue, O. Simonin, Interaction between a deformable buoyant bubble and a homogeneous isotropic turbulence, in: Conference on Turbulence and Interactions TI2006, May 29-June 2, 2006, Porquerolles, France, 2006.

[100] F.M. Denaro, What does finite volume-based implicit filtering really resolve in large-eddy simulations?, J. Comput. Phys. 230 (10) (2011) 3849–3883, https://doi.org/10.1016/j.jcp.2011.02.011, http://www.sciencedirect.com/science/article/pii/S0021999111000933.

[101] S.B. Lee, A study on temporal accuracy of OpenFOAM, Int. J. Nav. Archit. Ocean Eng. 9 (4) (2017) 429–438, https://doi.org/10.1016/j.ijnaoe.2016.11.007, http://www.sciencedirect.com/science/article/pii/S2092678216305465.

[102] J. Martínez, F. Piscaglia, A. Montorfano, A. Onorati, S. Aithal, Influence of spatial discretization schemes on accuracy of explicit LES: canonical problems to engine-like geometries, Comput. Fluids 117 (2015) 62–78, https://doi.org/10.1016/j.compfluid.2015.05.007.

[103] F. Piscaglia, A. Montorfano, A. Onorati, Development of a non-reflecting boundary condition for multidimensional nonlinear duct acoustic computation, J. Sound Vib. 332 (4) (2013) 922–935, https://doi.org/10.1016/j.jsv.2012.09.030.

[104] C. Brennen, Cavitation and Bubble Dynamics, Cavitation and Bubble Dynamics, Cambridge University Press, 2013, https://books.google.it/books?id=yRhaAQAAQBAJ.

[105] L. D'Agostino, S.I. Green, Simultaneous cavitation susceptibility meter and holographic measurements of nuclei in liquids, J. Fluids Eng. 114 (2) (1992) 261–267, https://doi.org/10.1115/1.2910025.

[106] S. Washio, 1 – review of cavitation nuclei, in: S. Washio (Ed.), Recent Developments in Cavitation Mechanisms, Woodhead Publishing, 2014, pp. 1–44, http://www.sciencedirect.com/science/article/pii/B978178242175750001X.

[107] A.K. Singhal, M.M. Athavale, H. Li, Y. Jiang, Mathematical basis and validation of the full cavitation model, J. Fluids Eng. 124 (3) (2002) 617, https://doi.org/10.1115/1.1486223.

[108] F. Nicoud, F. Ducros, Subgrid-scale stress modelling based on the square of the velocity gradient tensor, Flow Turbul. Combust. 62 (1999) 183–200.

[109] R.J. LeVeque, Numerical Methods for Conservation Laws, Lectures in Mathematics, ETH, Zurich, 2007.

[110] A. Harten, High resolution schemes for hyperbolic conservation laws, J. Comput. Phys. 135 (2) (1997) 260–278, https://doi.org/10.1006/jcph.1997.5713.

[111] J. Boris, D. Book, Solution of continuity equations by the method of flux-corrected transport, in: J. Killeen (Ed.), Controlled Fusion, in: Methods in Computational Physics: Advances in Research and Applications, vol. 16, Elsevier, 1976, pp. 85–129.

[112] S.T. Zalesak, Fully multidimensional flux-corrected transport algorithms for fluids, J. Comput. Phys. 31 (3) (1979) 335–362, https://doi.org/10.1016/0021-9991(79)90051-2.

[113] B. Biçer, A. Sou, Application of the improved cavitation model to turbulent cavitating flow in fuel injector nozzle, Appl. Math. Model. 40 (7) (2016) 4712–4726, https://doi.org/10.1016/j.apm.2015.11.049, http://www.sciencedirect.com/science/article/pii/S0307904X1500801X.

[114] F. Piscaglia, F. Giussani, A. Montorfano, J. Hélie, S. Aithal, A MultiPhase Dynamic-VoF solver to model primary jet atomization and cavitation inside high-pressure fuel injectors in OpenFOAM, Acta Astronaut. (2019), https://doi.org/10.1016/j.actaastro.2018.07.26.

[115] R. Clift, Bubbles, Drops, and Particles (Dover Civil and Mechanical Engineering), Dover Publications, 2005, https://www.xarg.org/ref/a/0486445801/.

[116] H. Wadell, Sphericity and roundness of rock particles, J. Geol. 41 (3) (1933) 310–331, http://www.jstor.org/stable/30058841.

[117] S. Osher, J. Sethian, Fronts propagating with curvature-dependent speed: algorithms based on Hamilton-Jacobi formulations, J. Comput. Phys. 79 (1988) 12–49, https://doi.org/10.1016/0021-9991(88)90002-2.

[118] S. Turek, Efficient Solvers for Incompressible Flow Problems, An Algorithmic and Computational Approach, Lecture Notes in Computational Science and Engineering, vol. 6, Springer, Berlin, 1999.

[119] N. Parolini, E. Burman, A finite element level set method for viscous free-surface flows, in: Applied and Industrial Mathematics in Italy, in: Proceedings of SIMAI 2004, World Scientific, Singapore, 2005, pp. 417–427.

[120] V. John, G. Matthies, MooNMD – a program package based on mapped finite element methods, Comput. Vis. Sci. 9 (2004) 1179–1195, https://doi.org/10.1016/j.apnum.2006.03.003.

[121] Physical aspects of the relaxation model in two-phase flow, Proc. R. Soc., Math. Phys. Eng. Sci. 428 (1875) (1990) 379–397, https://doi.org/10.1098/rspa.1990.0040, http://rspa.royalsocietypublishing.org/content/428/1875/379.full.pdf.

[122] P. Downar-Zapolski, Z. Bilicki, L. Bolle, J. Franco, The non-equilibrium relaxation model for one-dimensional flashing liquid flow, Int. J. Multiph. Flow 22 (3) (1996) 473–483, https://doi.org/10.1016/0301-9322(95)00078-X, http://www.sciencedirect.com/science/article/pii/030193229500078X.

[123] K. Neroorkar, B. Shields, R.O. Grover Jr., A. Plazas Torres, D. Schmidt, Application of the homogeneous relaxation model to simulating cavitating flow of a diesel fuel, in: SAE 2012 World Congress & Exhibition, SAE International, 2012.

[124] E. Winklhofer, E. Kull, E. Kelz, A. Morozov, Comprehensive hydraulic and flow field documentation in model throttle experiments under cavitation conditions, in: ILASS 2001, 17th European Conference on Liquid Atomization and Spray Systems, Zurich, Switzerland, 2001.
[125] F. Brusiani, S. Negro, G.M. Bianchi, M. Moulai, K. Neroorkar, D. Schmidt, Comparison of the homogeneous relaxation model and a Rayleigh Plesset cavitation model in predicting the cavitating flow through various injector hole shapes, in: SAE 2013 World Congress & Exhibition, SAE International, 2013.
[126] R.D. Reitz, Atomization and Other Breakup Regimes of a Liquid Jet, Ph.D. thesis, Princeton Univ., NJ, 1978.